NASA/TP-2019-220433
DOT/FAA/TC-19/29

Radar Detection of High Concentrations of Ice Particles – Methodology and Preliminary Flight Test Results

Steven D. Harrah
Langley Research Center, Hampton, Virginia

Justin K. Strickland and Patricia J. Hunt
AMA - NASA Langley Research Center, Hampton, Virginia

Fred H. Proctor
Langley Research Center, Hampton, Virginia

George F. Switzer
AMA - NASA Langley Research Center, Hampton, Virginia

Thomas P. Ratvasky
NASA Glenn Research Center, Cleveland, Ohio

J. Walter Strapp
Met Analytics Inc., Toronto, Ontario, Canada

Lyle Lilie
Science Engineering Associates, Tolland, Connecticut

Chris Dumont
FAA William J. Hughes Technical Center, Atlantic City, New Jersey

December 2019

NASA STI Program . . . in Profile

Since its founding, NASA has been dedicated to the advancement of aeronautics and space science. The NASA Scientific and Technical Information (STI) program plays a key part in helping NASA maintain this important role.

The NASA STI program operates under the auspices of the Agency Chief Information Officer. It collects, organizes, provides for archiving, and disseminates NASA's STI. The NASA STI program provides access to the NTRS Registered and its public interface, the NASA Technical Reports Server, thus providing one of the largest collections of aeronautical and space science STI in the world. Results are published in both non-NASA channels and by NASA in the NASA STI Report Series, which includes the following report types:

- TECHNICAL PUBLICATION.
  Reports of completed research or a major significant phase of research that present the results of NASA Programs and include extensive data or theoretical analysis. Includes compilations of significant scientific and technical data and information deemed to be of continuing reference value. NASA counter-part of peer-reviewed formal professional papers but has less stringent limitations on manuscript length and extent of graphic presentations.

- TECHNICAL MEMORANDUM.
  Scientific and technical findings that are preliminary or of specialized interest, e.g., quick release reports, working papers, and bibliographies that contain minimal annotation. Does not contain extensive analysis.

- CONTRACTOR REPORT.
  Scientific and technical findings by NASA-sponsored contractors and grantees.

- CONFERENCE PUBLICATION.
  Collected papers from scientific and technical conferences, symposia, seminars, or other meetings sponsored or co-sponsored by NASA.

- SPECIAL PUBLICATION.
  Scientific, technical, or historical information from NASA programs, projects, and missions, often concerned with subjects having substantial public interest.

- TECHNICAL TRANSLATION.
  English-language translations of foreign scientific and technical material pertinent to NASA's mission.

Specialized services also include organizing and publishing research results, distributing specialized research announcements and feeds, providing information desk and personal search support, and enabling data exchange services.

For more information about the NASA STI program, see the following:

- Access the NASA STI program home page at http://www.sti.nasa.gov

- E-mail your question to help@sti.nasa.gov

- Phone the NASA STI Information Desk at 757-864-9658

- Write to:
  NASA STI Information Desk
  Mail Stop 148
  NASA Langley Research Center
  Hampton, VA 23681-2199

NASA/TP–2019-220433
DOT/FAA/TC-19/29

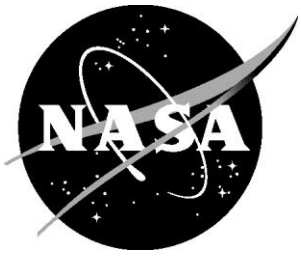

Radar Detection of High Concentrations of Ice Particles – Methodology and Preliminary Flight Test Results

Steven D. Harrah
Langley Research Center, Hampton, Virginia

Justin K. Strickland and Patricia J. Hunt
AMA - Langley Research Center, Hampton, Virginia

Fred H. Proctor
Langley Research Center, Hampton, Virginia

George F. Switzer
AMA - NASA Langley Research Center, Hampton, Virginia

Thomas P. Ratvasky
Glenn Research Center, Cleveland, Ohio

J. Walter Strapp
Met Analytics Incorporated, Toronto, Ontario, Canada

Lyle Lilie
Science Engineering Associates, Tolland, Connecticut

Chris Dumont
FAA William J. Hughes Technical Center, Atlantic City, New Jersey

National Aeronautics and
Space Administration

Langley Research Center
Hampton, Virginia 23681-2199

December 2019

Available from:

NASA STI Program / Mail Stop 148
NASA Langley Research Center
Hampton, VA 23681-2199
Fax: 757-864-6500

Abstract

High Ice Water Content (HIWC) has been identified as a primary causal factor in numerous engine events over the past two decades. Previous attempts to develop a remote detection process utilizing modern commercial radars have failed to produce reliable results. This paper discusses the reasons for previous failures and describes a new technique that has shown very encouraging accuracy and range performance without the need for any hardware modifications to industry's current radar designs. The performance of this new process was evaluated during the joint NASA/FAA HIWC RADAR II Flight Campaign in August of 2018. Results from that evaluation are discussed, along with the potential for commercial application, and development of minimum operational performance standards for a future commercial radar product.

Introduction

For the past 15 years, research scientists and engineers from across the globe and within government, industry, and academia have been studying an atmospheric condition where high concentrations of ice particles are produced. The atmospheric condition known in the US as High Ice Water Content (HIWC) has been identified as the primary causal factor behind many engine events [1]. These conditions are produced by persistent areas of strong, deep, convection in association with mesoscale convective systems and tropical storms. Encounters with HIWC produce a range of impacts on the flight deck and flight operations - from temporary loss of thrust to severe engine damage and loss of engine operation. The financial cost of these encounters is substantial; in addition to a few costly engine replacements that occur each year, these encounters cause additional inspections and maintenance, and require removal of the aircraft from operations for hours to days. Consequently, the FAA and airline industry desire a means to remotely detect, safely mitigate, and/or avoid these conditions while minimizing excessive disruption and economic consequences to the industry. This desire exists for both current and new aircraft, since reduced exposure is expected to remain a priority for commercial operations and increased safety even though future engines are likely be more ice tolerant.

Airborne weather radars are carried on all transport aircraft and are the single instrument capable of providing tactical detection and avoidance information to pilots regarding hazardous weather conditions. However, pilots that have encountered unexpected HIWC conditions have consistently described their radar display as indicating benign conditions – often black (no indication of severe weather) or at worst green (showing the presence of hydrometeors but implying benign/safe levels) [1, 2]. Post-flight analyses suggest ice concentrations in these regions should have an equivalent reflectivity of greater than 40 dBZ (red on a pilots weather radar display) – a flight condition pilots are trained to avoid. While HIWC conditions can occur in high radar reflectivity conditions, pilots already avoid these regions. A hypothesis put forward by Mason et al. [1, 2] was that these engine events were also being produced by high concentration of small ice crystals occurring in low radar reflectivity regions. For the purposes of this paper, and also as generally applied for many studies related to engine-event weather, the term HIWC is intended to encompass regions of high concentrations of ice within apparently-benign radar reflectivity.

The HIWC Project [3] was formed in 2006 to make in-situ measurements of deep convective clouds to support the assessment of a new FAA ice crystal environmental envelope Appendix D [4], also adopted by the European Aviation Safety Agency as Appendix P [5]. In 2010, the NASA Langley Radar Team joined the HIWC Project to investigate the performance of airborne weather radars in HIWC conditions, and then recommend any changes to this technology that would enable HIWC detection. In 2012, the

High Altitude Ice Crystals (HAIC) Project [6] joined in collaboration with the HIWC Project to conduct the HAIC-HIWC Flight Campaigns in deep convective clouds in Darwin, Australia (in 2014) and Cayenne, French Guiana (in 2015). Later in 2015, NASA and the FAA conducted the HIWC RADAR I Flight Campaign [7], to investigate the response of commercial airborne weather radars to hazardous HIWC conditions with a secondary objective of providing supplemental in-situ cloud measurements to those collected during the HAIC-HIWC Flight Campaigns. Data from this flight campaign was then used to develop an explanation for why existing radars were not detecting hazardous HIWC conditions. The data then provided a testbed from which multiple algorithms were assessed and the flight candidate algorithm was developed for demonstration during the 2018 NASA/FAA HIWC RADAR II Flight Campaign [7].

This paper describes the various radar observables associated with HIWC detection and postulates how each could offer insight into HIWC detection. The theoretical basis for the new process is provided and perceived issues are also presented. The paper concludes with flight evaluations and preliminary results assessing the performance of these algorithms with particular attention to this new algorithm and future work into the remote detection of HIWC.

Radar Observables as an Ice Water Content Metric

Modern airborne Doppler weather radar systems are capable of long range, remote detection of many atmospheric phenomena. The amplitude and frequency of radar echoes are used to make remote measurements of weather conditions such as heavy rain, turbulence, and windshear. Most commercial systems operate at a single X-band frequency and single polarization, although future systems may utilize multiple frequencies and/or dual polarization. The HAIC-HIWC Flight Campaigns [6] and the joint NASA/FAA HIWC RADAR Flight Campaigns [7] have confirmed the hypothesis established by Mason et al [1] that HIWC conditions are characterized by high concentrations of small ice particles. Thus identifying radar parameters that are sensitive to high concentrations of small ice particles became essential for remote detection of HIWC conditions. The following sections describe relevant radar observables and their applicability for HIWC detection and Ice Water Content (IWC) estimation.

Radar Reflectivity

Radar reflectivity is a measure of the amplitude of reflected power as a fraction of the incident power. Ice water content retrieval from radar reflectivity has been examined previously [8, 9]. In some cases temperature was included in the relationship [10, 11] in an attempt to identify a discriminator for HIWC detection. Previous investigations primarily focused on W-band radar measurements, which produces different scattering results than those observed with commercial X-band radars. A notable exception are the X-band results by Heymsfield et al. [12]. However, none of these previous investigations: used a commercial airborne weather radar, targeted deep convective systems seeking HIWC conditions, or used IWC measurements to derive relationships exceeding 1 g/m^3.

For water droplets, the relationship between radar reflectivity and water content is well-understood. In pulsed weather radar systems, Radar Reflectivity Factor (RRF) is usually computed using the mean signal amplitude of all pulses in a Coherent Processing Interval (CPI). For Rayleigh-scattering sized particles, RRF is defined [13] as the sum of all drop diameters raised to the sixth power contained in a unit volume (i.e. $RRF \equiv \left(\frac{1}{\Delta V}\right)\sum_i D_i^6$), whereas total water content (TWC) in the same unit volume is proportional to the sum of the volume of all of the drops (i.e. $TWC = \left(\frac{\rho\pi}{6}\right)\left(\frac{1}{\Delta V}\right)\sum_i D_i^3$) which depends on the cube of the drop diameters. This means that the RRF is dominated by the larger drops much more so than TWC.

For ice particles, an equivalent RRF may be estimated if the Particle Size Distribution (PSD) is known. The PSD describes the number of particles (N) of a given diameter (D). Equivalent RRF and TWC are easily computed using mass-equivalent water droplets. For irregularly shaped ice particles, one must estimate the particles' masses using a mass-size relationship (e.g. Locatelli and Hobbs [14]) and account for the different densities and dielectric factors between water and ice (Smith [15]).

For nominal size distributions (e.g. Marshall Palmer [16] for rain or Marshall Gunn [17] for snow), the number of large particles in the atmosphere increases with precipitation rate, which means that RRF and TWC both increase. An overall increase in the concentration of particles across every size-bin results in an increase in both RRF and TWC (Figure 1A). If nature behaved only in this manner, RRF would be a reliable discriminator of hazardous and non-hazardous rain and ice particle conditions, but it does not.

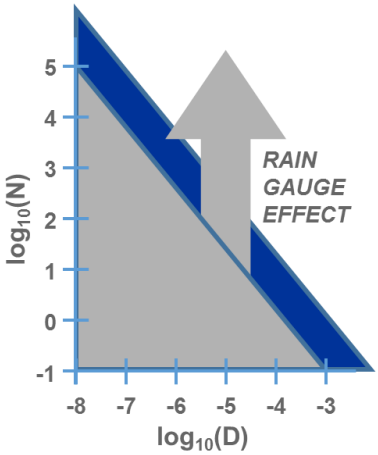

Figure 1A: Effect of Increasing Precipitation Rate on Particle Size Distribution

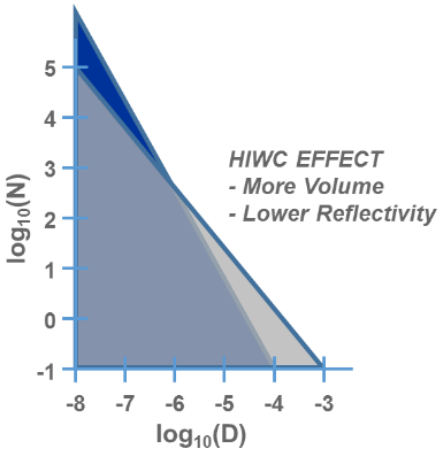

Figure 1B: Effect of HIWC Conditions on Particle Size Distribution

It is believed, in HIWC conditions, the PSD shifts to higher concentrations of small particles without a corresponding increase of large particles (Figure 1B). This PSD can result in significant amounts of IWC yet low RRF. Therefore, hazardous ice concentrations can appear benign according to standard RRF classification. As will be demonstrated later in this study, attempts to estimate IWC or discriminate hazardous from non-hazardous IWC conditions using RRF (including the added use of temperature) have been unsuccessful as the correlation does not result in a functional relationship, but instead, a single RRF maps into a wide range of IWC.

Multi-frequency

Multi-frequency detection of HIWC relies upon the scattering differences of ice particles at two (or more) radar frequencies. These scattering differences can be due to changes in material properties (i.e., refractive index) or due to particle sizes (e.g., Rayleigh vs Mie scattering) or both. These differences must be significant so that the PSD can be unambiguously estimated.

It is believed that making radar observations using more than a single radio frequency (RF) band can provide enough additional information for effective discrimination of hazardous and non-hazardous icing conditions [18]. For example, ground based observations have shown that the PSD of ice-phase clouds composed of dry crystals or aggregates can be estimated using multi-frequency radar measurements (Sekelsky et al. [19]). If adapted to airborne weather radars, this technique could provide an estimate of IWC in similar conditions.

The introduction of multiple frequencies requires new radar systems, new aircraft radomes, and possibly other hardware changes. FAA certification of these systems would also be required. Though multi-frequency airborne radar systems could provide additional benefits beyond HIWC detection, at this time they are considered a cost-prohibitive solution for the commercial aviation industry.

Polarimetric

Polarimetric radar utilizes asymmetries in particle scattering characteristics to ascertain information on the shapes and sizes of particles. Particles that have significant differences in the particle dimensions can produce significant difference in their backscatter power (i.e., differential reflectivity, Z_{DR}). While there is some evidence that HIWC has a weak Z_{DR} signature, there are other polarimetric signatures that have been shown to have a stronger correlation with HIWC. Nguyen et al. [20] describe a methodology for IWC retrieval using specific differential phase (K_{DP}) measurements weighted by Z_{DR}.

Linear Depolarization Ratio (L_{DR}) is a polarimetric measure of how much an incident polarized wave is depolarized during its interaction with the ice particle(s). It is hypothesized that this depolarization occurs, in HIWC conditions, because the polarized wave interacts many times, with many particles during the backscatter process. Whereas in non-HIWC conditions (producing the same backscatter power) the backscattered wave characteristic is dominated by fewer interactions with larger particles.

Fully-polarimetric radars typically consist of two independent transmit and receive channels – one for each polarization. The need for additional hardware and extensive modifications required to enable full polarimetric radar measurements is considered cost-prohibitive and eliminates fully-polarimetric radar from current consideration. Slightly less capable designs that utilize changing polarization from pulse to pulse are far less costly and offer almost as many benefits.

Making polarimetric measurements of HIWC conditions was a primary objective of the 2018 HIWC RADAR II Flight Campaign [7]; however, manufacturing issues arose too late to overcome to add this capability for those flight tests. The desire for these measurements remains an area of interest for further study and future flight campaigns.

Swerling Process

In the early 1950's, Peter Swerling developed a method for statistically modeling radar targets that appeared to have rapidly changing Radar Cross Section (RCS) values when measured by pulsed radar systems [21]. He devised four classes of what he called "fluctuating targets" that later became known as "Swerling targets." A fluctuation target results in pulse to pulse variability in the signal amplitude of the radar return echoes.

While the Swerling target models are for approximating point targets (i.e. targets with physical dimensions much smaller than the radar resolution volume), weather is a distributed target (i.e. much larger than the radar resolution volume). Based on the 2015 HIWC RADAR I Flight Campaign, NASA identified that HIWC weather conditions exhibited a significant amount of variability in signal amplitude from pulse to pulse. At this time, it is hypothesized that this rapid variability results from changing constructive and destructive interference in the return signals from the relative distance to the many particles and the motion of the aircraft, which is similar to the process that causes the observed de-polarization. The fluctuating signal amplitude is exploited to discriminate HIWC conditions from other non-hazardous icing conditions – this is referred to in this paper as the "Swerling process", in homage to Peter Swerling and his ground breaking work related to this observable.

The Swerling process for HIWC detection relies on the signal amplitude, but unlike standard radar reflectivity, it accounts for the statistical variance in amplitude as well as the mean amplitude within a CPI. With sufficient pulses in a CPI, it is possible to compute the Index of Dispersion (I_D) of the pulse amplitudes, which is the ratio of the variance to the mean:

$$I_D = \frac{\sigma^2}{\mu}$$

Using RRF as the range independent measure of amplitude, the index of dispersion has the same units as RRF but is a normalized measure of the variance in RRF rather than RRF itself.

A major benefit of the Swerling technique is that it can be implemented without any hardware modifications to existing commercial airborne weather radar systems; only software changes are necessary. Consequently, it is the lowest cost option for implementing a HIWC detection capability. Subsequent capabilities available in future generations of radar systems (e.g. multi-frequency or polarimetric) may eventually supplant the Swerling process; however, no commercial systems currently exist nor are the technology modifications available for rapid, wide-spread deployment into the current generation of radar systems.

Theoretical Evaluation

While it was found that HIWC weather conditions result in pulse to pulse fluctuations in received radar signal amplitude, it is also known that turbulent weather conditions can likewise cause variability in radar echoes, so it is important to understand if turbulence alone can result in false indications of HIWC using the Swerling process. Turbulence is often estimated by measuring the Doppler frequency variance (i.e. spectral width) in radar return signals, however it also manifests as signal amplitude fluctuations. To assess the impact of turbulence on the Swerling process, fundamental simulations were performed where noiseless signals were modeled with and without amplitude and/or spectral variance and the amplitude index of dispersion computed.

In-phase and quadrature sinusoidal components of return signal samples were computed as follows:

$$I(t) = \sum_{i=1}^{N} A(t)\cos(2\pi f_i t) \quad \text{and} \quad Q(t) = \sum_{i=1}^{N} A(t)\sin(2\pi f_i t)$$

where the signals are composed of N normally distributed spectral components (f_i) and the amplitude may vary with time ($A(t)$). The independent variable spectral width defines the standard deviation of the frequency distribution, while amplitude is a normal random variable defined by the mean (μ) and standard deviation (σ) for a given index of dispersion. Time samples are computed for each pulse at a given Pulse Repetition Interval (PRI) (i.e. $I_j = I(PRI*j)$ and $Q_j = Q(PRI*j)$, for $j = 0 \ldots$ number of pulses - 1).

With the amplitude of the modeled signal held constant, representing a perfectly constant mean RRF with no RRF variance, it was found that the sampled, signal amplitude, index of dispersion exhibits an inverse exponential relationship with spectral width (Figure 2). At low spectral width values, representative of little or no turbulence, the resulting amplitude I_D is very small, regardless of the mean amplitude. With increasing spectral width, I_D increases asymptotically approaching the mean signal amplitude as spectral width nears the Nyquist frequency – half of the Pulse Repetition Frequency (PRF) – where higher spectral width is representative of more significant turbulence.

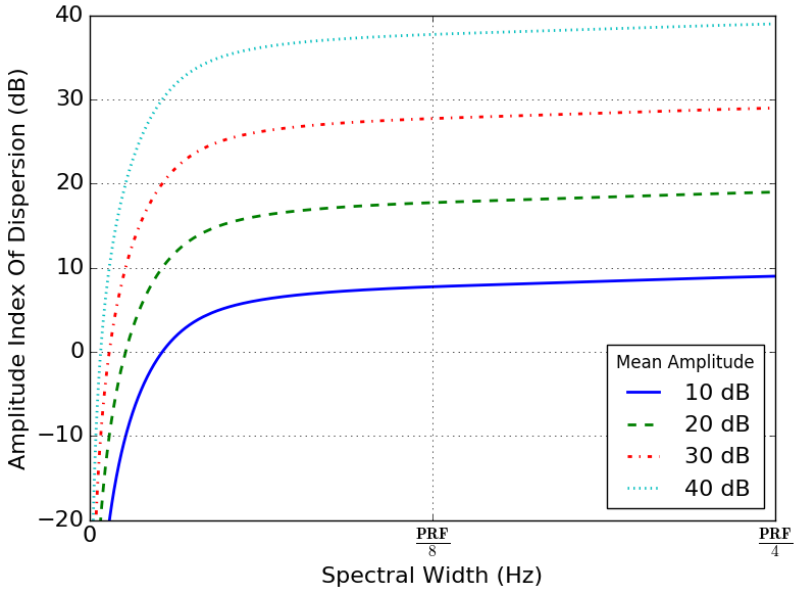

Figure 2: Impact of Spectral Width on Amplitude Index of Dispersion

If the amplitude of the modeled signal is varied, representing a fluctuating target, it was found that the sampled, signal amplitude, index of dispersion appropriately quantifies the amplitude variance as long as it is greater than the contribution from spectral width (Figure 3). Consequently, the amplitude index of dispersion measurement is the maximum value from either a fluctuating target or turbulence, whichever has the greater impact.

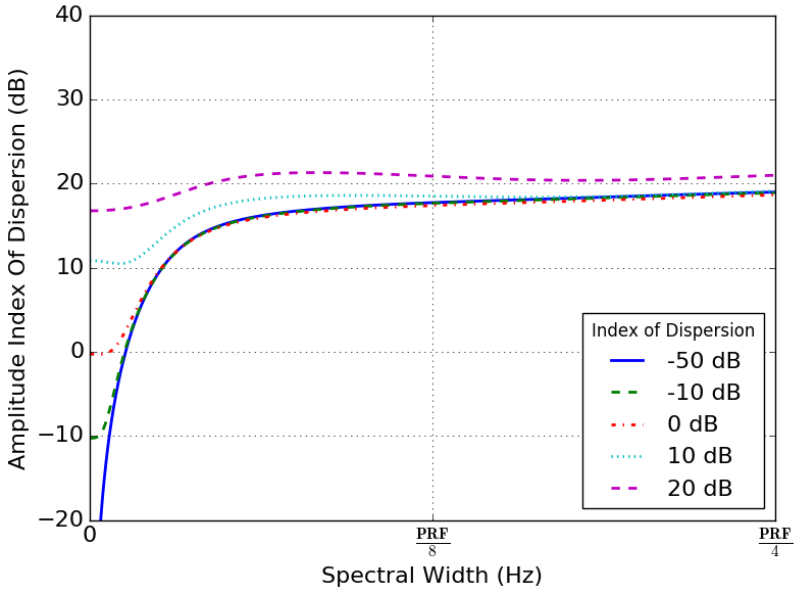

Figure 3: Impact of Fluctuation Targets on Amplitude Index of Dispersion

At low spectral width values, representative of little or no turbulence, the resulting amplitude index of dispersion characterizes the fluctuating target. At high spectral width values, representative of more turbulent conditions, the resulting amplitude index of dispersion may be indicative of turbulence if target

fluctuations are less significant. Conversely, variance in the signal amplitude will have a similar impact on spectral width estimates made by spectral processing techniques – e.g. Fast Fourier Transform (FFT) or Pulse-Pair Processing (PPP).

In flight conditions with little or no turbulence but with a high amplitude index of dispersion, spectral width measurements will be greater than what otherwise would be indicative of the actual turbulence levels. This cross-coupling is worth noting but may not impact an operational capability, as it may not be necessary to distinguish between a HIWC hazard and a turbulence hazard when either hazard should be avoided.

Results from this simulation show that the signal amplitude index of dispersion does increase with increasing spectral width; therefore, a HIWC detection algorithm based on RRF index of dispersion can be impacted by turbulence. Higher turbulence levels may bias IWC estimates; however, in this scenario the aircrew may want to avoid these areas as well due to their turbulent conditions. In areas where the turbulence spectral width is less than the amplitude variance due to HIWC, the RRF index of dispersion provides an accurate estimate of IWC. Examples of these results, taken from recorded flight data are shown in the results section. Conceivably, an operational HIWC detection algorithm based on this Swerling technique would work in conjunction with existing turbulence detection algorithms and display systems to minimize false indications.

Flight Evaluation

In order to test these concepts and collect needed HIWC data, NASA has conducted two flight campaigns utilizing the NASA DC-8 Airborne Science Laboratory (NASA 817). The aircraft is based out of the NASA Armstrong Flight Research Center (AFRC) and housed/maintained at the AFRC Building 703, located in Palmdale, California. The flight campaigns were conducted to measure/characterize the HIWC ice crystal environment and to develop/demonstrate radar-based techniques to help the commercial airlines identify areas of the high ice crystal concentrations [7].

The first flight campaign, flown in 2015, was mainly used to collect weather radar measurements/signatures of HIWC conditions. Along with the radar, other meteorological instruments were installed onto the DC-8. Cloud probe instruments provided by NASA Glenn Research Center (GRC) were mounted onto wing pylons to use as in-situ reference data of the environment through which the aircraft flew. These data were then analyzed to compare the radar measurements with the probe measurements to establish detection signatures and identify methodologies that offered promising performance as potential commercial detection processes.

Utilizing these measurements, a variety of algorithms were studied to assess their success and difficulties discriminating HIWC from benign IWC conditions. These algorithms considered traditional processes that often focused on RRF as the primary measure of IWC, but also considered less traditional processes like those often used in polarimetry where an observable is correlated with a desired physical measurement. The result of this study was a ranked list of algorithms to assess in future flight campaign(s).

The second flight campaign, conducted in August of 2018, was flown to assess the performance of each candidate radar algorithm's ability to predict HIWC conditions, determine the accuracy of ice water content estimates, and localization of the HIWC environment. A more detailed summary of these flight campaigns and the data collected is provided in Ratvasky et al. [7].

NASA DC-8 with HIWC Instrumentation

The NASA DC-8 aircraft was outfitted with a variety of instruments to measure the HIWC environment. The DC-8 was equipped with a Honeywell RDR-4000 Commercial Off The Shelf (COTS), X-band weather radar, modified by Honeywell to provide raw radar measurements and a data recording subsystem. Multiple atmospheric probes were also installed in order to record the actual meteorological conditions in which the aircraft flew.

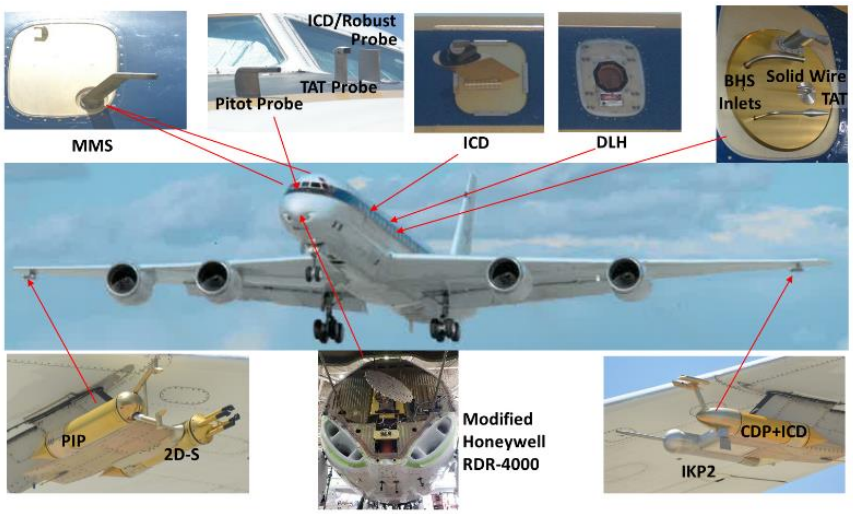

Figure 4: HIWC RADAR II Instrumentation on NASA AFRC DC-8 flying laboratory

The suite of primary probes included a second-generation Iso-Kinetic Probe (IKP2) for measuring ice water content and three particle probes for measuring particle size distribution: the Cloud Droplet Probe (CDP-2), the 2-Dimensional Stereoscopic (2D-S) imaging probe, and the Precipitation Imaging Probe (PIP). The IKP2 was developed by the HIWC team specifically to measure bulk Total Water Content (TWC)[†] in the high speed/altitude/concentration environment to an accuracy of 20% [22, 23], and was also used in the two HAIC-HIWC flight campaigns [6]. The CDP-2, 2D-S, and PIP are all modern airborne cloud probes commonly used by the atmospheric science community. Other supporting probes installed onto the aircraft included research Total Air Temperature (TAT) probes, three TWC hot wire probes mounted at various locations to study TWC differences, background humidity systems, and pitot probe and flow direction probes. Figure 4 shows the installation locations of the instruments that were used on the 2018 flight campaign (with a complete description available in Ratvasky et al. [7]).

RIWC Algorithm Implementation

Analysis of the radar and IKP2 measurements collected during the 2015 HIWC RADAR I Flight Campaign identified the correlation between IWC and the I_D for RRF. Using this correlation, the Radar-estimated IWC (RIWC)[††] was calculated from the I_D for RRF. During the 2018 HIWC RADAR II Flight Campaign, a data acquisition system connected to the RDR-4000 radar processor recorded the unprocessed radar return signals (i.e. "In-phase and Quadrature" (I&Q) sample data) and forwarded them to research systems which performed real-time signal and data processing to compute and display the radar measurements; including RIWC.

[†] *Mixed phased was rarely observed during the HIWC RADAR Flight Campaigns, so TWC measurements by the IKP2 are approximately the same as IWC.*

[††] *The term RIWC is used specifically for IWC derived from the NASA-developed "Swerling algorithm".*

The research displays presented radar measurements in a Plan Position Indicator (PPI) format similar to the standard cockpit Radar Indicator or (as was used in the DC-8) a Multi-Function Display (MFD). The primary difference was that these research displays were configurable and could provide additional information not on the pilot's MFD.

RIWC is computed/calculated as follows, the mean magnitude of the radar return signal is given by:

$$\mu = \frac{1}{n}\sum_{i=1}^{n}\left(I_i^2 + Q_i^2\right)$$

where n is the number of valid pulses in the CPI. This mean magnitude represents the received echo average power which is used to estimate RRF using the radar range equation for weather targets [13]. For processing efficiency, the variance of the signal magnitudes is likewise computed within the same summation:

$$\sigma^2 = \left(\frac{1}{n}\right)\sum_{i=1}^{n}\left(I_i^2 + Q_i^2\right)^2 - \mu^2$$

With the proper unit conversions to represent the received signal magnitude as RRF – which is range independent – the I_D is then computed as the ratio of these two results. This ratio can be expressed in units of dBZ as.

$$\Phi_D = 10\log_{10}(I_D) = 10\log_{10}\left(\frac{\sigma^2}{\mu}\right)$$

It was found that IWC in units of g/m^3 could be estimated reasonably well using a simple empirically derived proportionality constant (10 g/m^3/dBZ), thus:

$$RIWC \approx \frac{\Phi_D}{10} = \log_{10}\left(\frac{\sigma^2}{\mu}\right)$$

This process is repeated for each range bin within the CPI and across all azimuth angles to produce RIWC PPI displays.

To filter out thermal noise, a threshold is applied on a pulse-by-pulse basis within a CPI. The signal to noise ratio (SNR) is computed and compared against a pre-determined processing threshold to exclude any pulses which fail to meet the minimum acceptable SNR from the summation. Consequently, the number of valid pulses in the CPI (n) may be less than the total number of pulses transmitted by the waveform. To estimate RRF, a single valid pulse ($n \geq 1$) is sufficient. However, to compute the variance and thus estimate RIWC, at least two valid pulses are required ($n \geq 2$).

As the radar antenna sweeps in azimuth, the angle traversed from one CPI to the next is less than one beamwidth. The overlapping measurements from sequential CPI's are averaged over the width of the antenna beam using a SNR weighted mean. Any CPI with insufficient SNR to meet the processing threshold is excluded.

The RDR-4000 radar is equipped with several different waveforms used depending on the operating mode and conditions. Furthermore, a firmware upgrade applied to the radar installed on the DC-8 prior to

the 2018 HIWC RADAR II Flight Campaign supplanted the waveforms employed during the 2015 HIWC RADAR I Flight Campaign. The differences in the various waveforms used include the number of pulses in a CPI, the PRF, the pulse length, and the application of (or not of) pulse compression techniques. Analysis of the RIWC results from the various waveforms show no discernable difference in the efficacy of the RIWC algorithm due to differing waveform parameters.

Because the RDR-4000 radar is a Minimum Equipment List (MEL) safety item and the RIWC algorithm is research-grade information, RIWC was implemented in a separate research processing system. No attempt was made to modify the radar system from its COTS configuration. Lastly, the radar is capable of making basic measurements out to 300 Nmi; however, only a limited amount of data could be provided over the data buses to the research processor so only 40 Nmi was available for the 2015 HIWC RADAR I Flight Campaign and 60 Nmi for the 2018 HIWC RADAR II Flight Campaign. These limitations apply to the research system and not to any theoretical/experimental limit of RIWC.

Summary of HIWC Radar II Flights

The HIWC Radar II Flight Campaign conducted in August 2018 completed 55 flight hours over seven research flights (Table 1). All of the flights were flown during daylight hours and targeted oceanic storm systems. Flight altitudes were chosen according to a pre-deployment sampling strategy [7] and only altered due to conditions encountered within each storm system or radar observations ahead of the aircraft. A summary of flight tracks and time histories for each flight is provided in Ratvasky et al. [7]; summary mosaics of radar imagery are included in this document's appendix.

Table 1: HIWC Radar II Flight Summary

#	Date	Duration (Min)	Type and Location
3	08/02/18	298	MCS, Eastern Gulf of Mexico
4	08/06/18	326	Convection, Southern Gulf of Mexico
6	08/15/18	609	TS Lane, Eastern Pacific
7	08/16/18	612	TS Lane, Eastern Pacific
8	08/18/18	465	Hurricane Lane, Eastern Pacific
9	08/19/18	416	Hurricane Lane, SE of Hawaii
10	08/20/18	553	Hurricane Lane, SE of Hawaii

The first two research flights (#3 & #4) were conducted from Fort Lauderdale/Hollywood International Airport (KFLL). These flights targeted oceanic convective systems in the central and southern Gulf of Mexico (Figure 5). These storms tended to be scattered with active areas of convection separated by hundreds of miles.

The remaining research flights were conducted from Palmdale Regional Airport (KPMD) and/or Kona International Airport (PHKO). These targeted a tropical system in the Eastern Pacific that developed into Tropical Storm and Hurricane Lane (Figure 6). The system first organized as a tropical depression, late on August 14th, and intensified into a tropical storm just prior to the first flight into the system on August 15th. The tropical storm was again encountered on the 16th, just several hours before intensifying into a hurricane. As the storm moved steadily westward it rapidly intensified into a major hurricane that later threatened the Hawaiian Islands. Hurricane Lane was well organized with a clearly defined eye,

surrounded by a concentric eye wall of deep convection and with inflowing feeder bands. A large upper-level cloud canopy surrounded the eye, as typical for major hurricanes. During the last three flight days, Lane was encountered (August: 18th, 19th, and 20th) while it was a Category 3 and 4 hurricane.

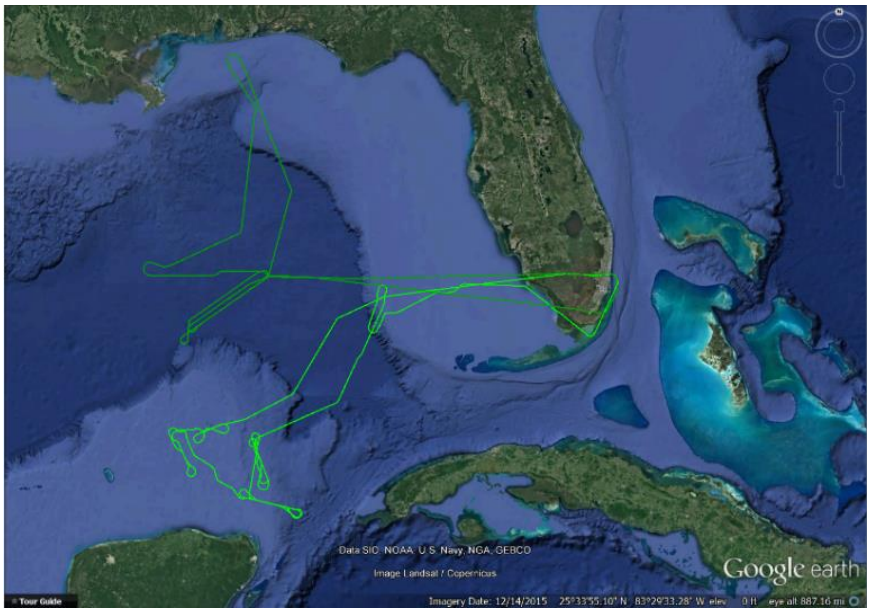

Figure 5. Flight Tracks for August 02 (Dark Green) and August 06 (Light Green)

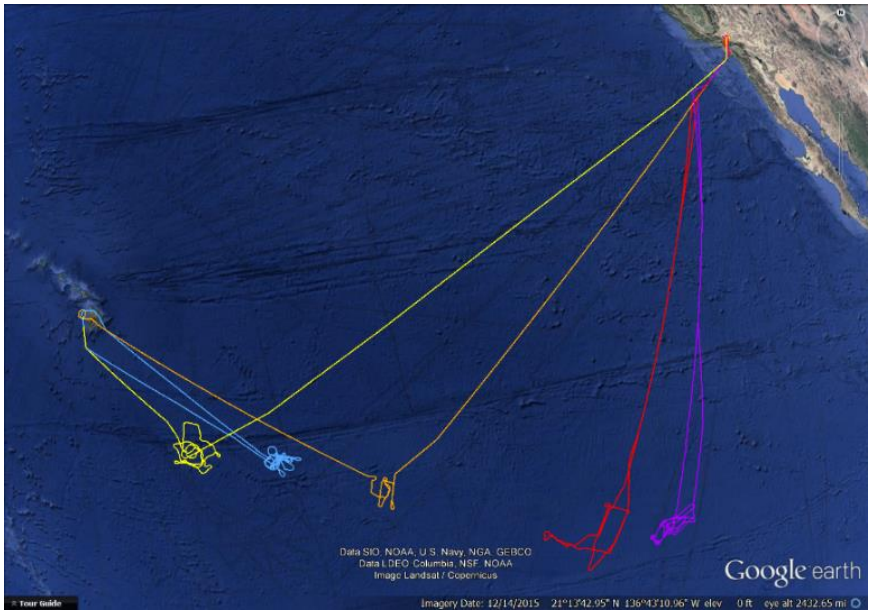

Figure 6. Flight Tracks for August 15, 16, 18, 19, & 20
(Magenta, Red, Orange, Cyan, & Yellow, respectively)

Due to the long transits required to reach these storm systems, not all of the available research flight hours were spent collecting relevant science data. In total, about 35 hours were flown within the storm systems (Table 2). Flight tracks within the storms were chosen based on guidance from ground support personnel using all available meteorological information (e.g. weather satellite products) and the onboard

airborne weather radar. The aim was to target areas predicted to contain HIWC conditions while avoiding hazards such as lightning, hail, turbulence, and "red" radar reflectivity as defined in the mission rules [7].

Table 2. HIWC Radar II Flight Campaign – In Cloud Data Summary

				Duration of IWC > 1g/m^3	
#	Date	Total time in cloud (min)	Max IWC (g/m^3)	Max (min)	# Runs > 1 min
3	08/02/18	219	3.1	7	6
4	08/06/18	204	2.9	1.6	3
6	08/15/18	375	2.8	6.7	7
7	08/16/18	389	3.7	2.9	8
8	08/18/18	258	2.0	1.7	2
9	08/19/18	276	3.6	1.9	1
10	08/20/18	372	2.9	3.4	3

The IWC measurements made by the IKP2 [22, 23] are used as reference values for radar post processing analyses. A summary of the in-cloud environment and maximum value of IWC over a distance scale of approximately 0.5 Nmi observed for each research flight in 2018 is shown in Table 2. This summary shows the maximum IWC reached for all days was on August 16th with an IWC value of 3.7 g/m^3. The hazard posed to an aircraft by a HIWC encounter is exacerbated by the duration of the exposure; therefore, Table 2 shows the duration of encounters with IWC greater than 1 g/m^3 and the number of times each day the aircraft endured IWC greater than 1 g/m^3 for longer than 1 minute. The longest endurance, during the 2018 flight campaign, was seven minutes, which occurred on August 2nd.

RIWC Performance

Estimates of RIWC were presented on the research radar displays during the 2018 flight campaign and were used to tactically guide the aircraft. It was often observed that IWC measurements made by the IKP2 corresponded with predictions made by the RIWC measurements during flight [7]. This provided a preliminary real-time qualitative assessment of the performance of the technique. Post-flight analysis of the recorded data, after quality assurance (QA) processes have been applied, seeks to produce a more quantitative assessment of the RIWC performance.

Analysis Methodology

Because the COTS weather radar was considered both standard avionics equipment included on the MEL and a scientific instrument, the science objectives could not impede flight safety; therefore, the radar generated normal volumetric scans to provide the flight crew with maximum situational awareness. This was deemed acceptable for research purposes since the main goal was to assess the efficacy of detecting HIWC conditions using a weather radar during normal operating conditions.

The radar produces remote measurements of the atmosphere ahead of the aircraft; whereas the other scientific instruments (i.e. IKP2, particle sizing probes, etc.) produce in-situ measurements. Consequently, careful translation and rotations of the remote measurements must be performed in order to associate radar measurements with subsequent in-situ measurements. Temporal differences between the time of measurement for radar data versus in-situ data must be taken into account. Special care was taken in the

comparative process to account for these spatio-temporal disparities.

Another complicating factor is the disparity in radar and cloud probe sample volumes. Radar measurement volumes grow with distance from the aircraft and exceed a cubic kilometer of sky after only a short distance ahead of the aircraft. Whereas cloud probe measurements are produced from about a square centimeter in cross-sectional area but can have integrated/averaged values for paths up to a kilometer in length/duration. These sample volume disparities add spatial complications to the comparisons.

The flight paths flown were not straight lines but looped around within the storm system, consequently the aircraft often passed through or near the same location multiple times, sometimes separated by many minutes or even hours. In order to maintain proper association of the appropriate radar and cloud probe measurements, a time limit is placed on the ensuing aircraft positions so that only in situ measurements over the next few minutes can be associated with radar measurements from the current scan. In-situ measurements from later transits of this space can/will be associated with radar measurements during those time periods. The time limit was chosen depending on the aircraft airspeed and the maximum range chosen for the analysis (i.e., $t_{max} \approx R_{max}/400$ kts).

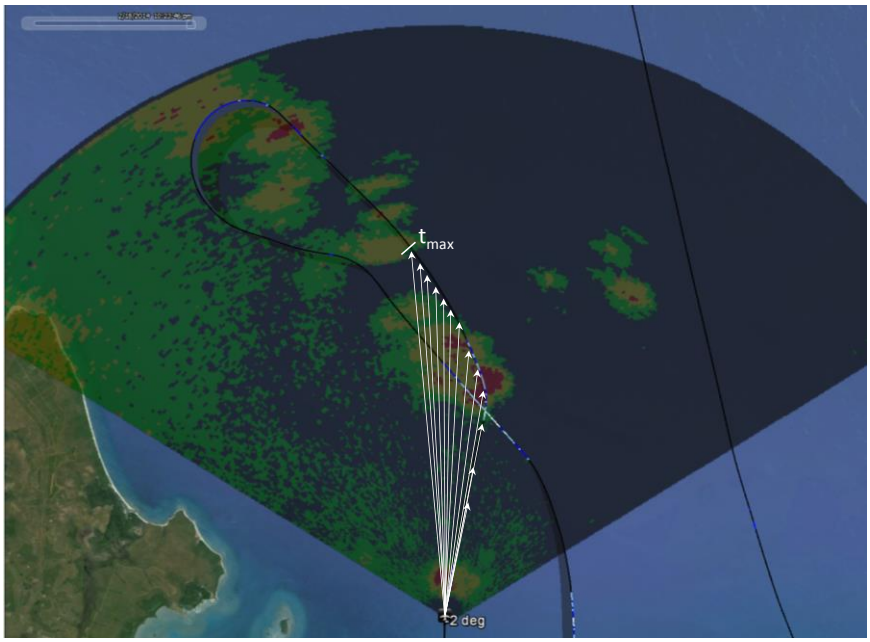

Figure 7. Associating an Aircraft Position to All Subsequent Cloud Probe Measurements (within time limit) via Line-of-Sight Vectors

The sample areas of the in-situ probes were small enough that the cloud probe measurements were considered point measurements made at specific intervals along the flight track. Conversely, individual radar measurements represent a much larger volume of space defined by the beam shape and waveform. The association process accounts for this by computing a line-of-sight vector from an aircraft position to all subsequent cloud probe measurement positions (Figure 7) within the time limit and determining if that vector falls within the radar beam (Figure 8). If so, the corresponding radar measurement is declared a candidate and tabulated for further consideration. This process is repeated for every aircraft position and radar CPI.

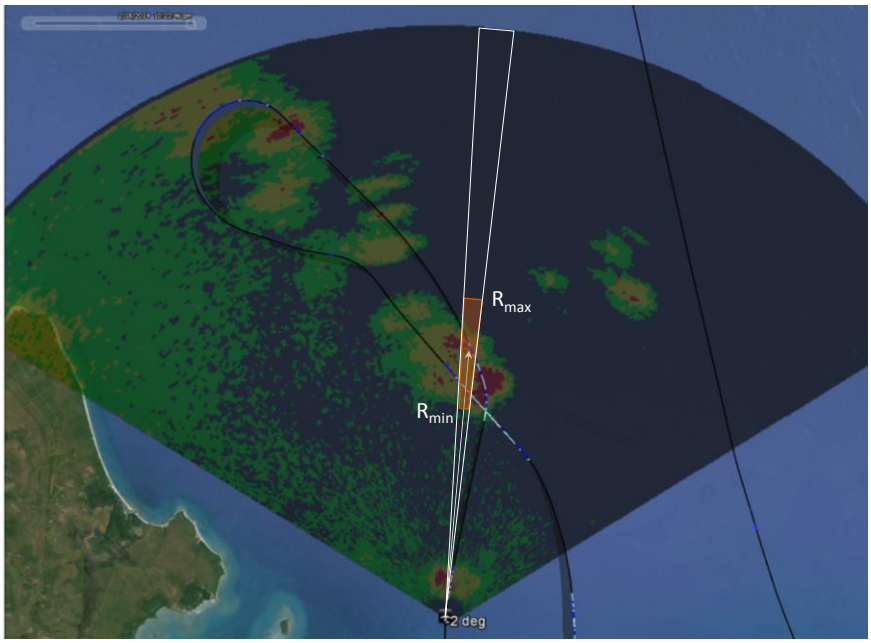

Figure 8: Remote Radar Measurements (within Range Limits) Associated with Cloud Probe Measurements

This approach can result in associating multiple radar measurements with a given cloud probe measurement location. The candidate results are first filtered by range to discard any that do not meet pre-defined range windows. The remaining candidates are then combined in cross-range to account for overlapping radar beams and to reduce the samples to one candidate per radar sweep per probe measurement. Finally, a single representative radar measurement is computed using the signal-to-noise ratio (SNR) to compute a weighted mean radar measurement for each probe measurement (1 Hz) within a sliding 5-second window along the flight track (i^{th} time sample shown in Figure 9). The end result is a one-to-one correspondence between radar and in-situ measurements with comparable spatial resolution.

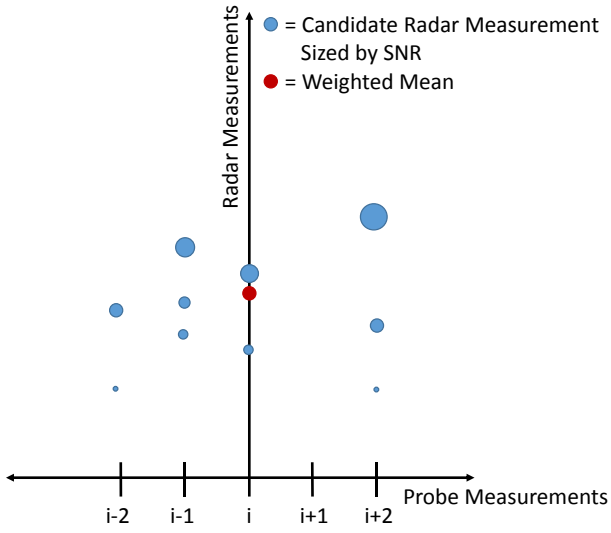

Figure 9: SNR Weighted Mean Radar Measurement for the 5-Second Window Associated with the i^{th} Cloud Probe Measurement

In order to analyze any range sensitivities, the correlation process was repeated for several radar measurement ranges. Due to the volumetric scan pattern performed by the radar, the radar beam did not revisit a given location every sweep, and maybe only once per volume scan. The range window was chosen to maximize the number of radar measurement samples while concentrating samples near the desired range.

Analysis Results

Preliminary analysis of the measurements collected during the HIWC RADAR Flight Campaigns focused on three areas of primary importance: assessment of the efficacy of detecting HIWC conditions using RRF, appraisal of the Swerling algorithm and resulting RIWC compared to measured IWC, and evaluation of the impact on the Swerling algorithm from turbulence (as indicated by spectral width estimates).

- Assessment of RRF

In normal rain and snow conditions, the RRF increases predictably with precipitation rate and provides a reliable estimate of water mass per volume of air (i.e. hazardous versus non-hazardous conditions). Analysis of the RRF measurements associated with the IKP2 measurements for both HIWC RADAR Flight Campaigns corroborate the pilot accounts of benign radar indications prior to HIWC encounters [1, 2]. In all of the observed HIWC conditions the radar MFD would have displayed black (RRF < 20 dBZ) or green (20 < RRF (dBZ) < 30) at most; even at the closest possible radar ranges providing the best spatial resolution and highest SNR (Figure 10).

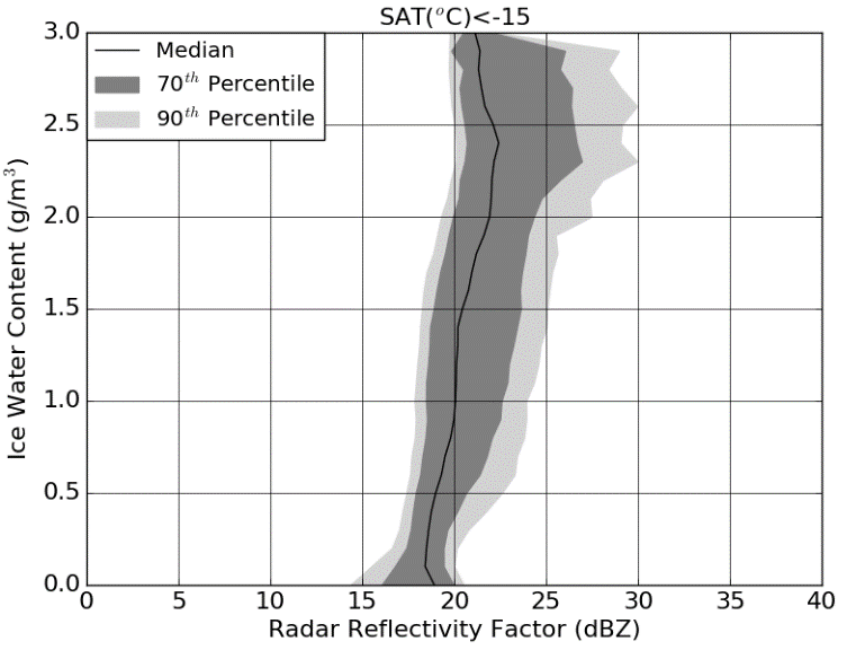

Figure 10: Relationship between X-Band RRF and IWC at Close Range for 2015 and 2018 Flights

Unlike rain, there is no significant increase in RRF corresponding with increasing IWC in HIWC conditions. Further, there is little to no distinction between RRF measurements from low to high IWC levels. The median RRF changes by no more than five dB over the entire range of IWC measurements, and a given RRF value (e.g. 20 dBZ) can be associated with nearly any IWC value. This non-functional

relationship between RRF and IWC is consistent regardless of the range at which the radar measurements are made.

A further attempt was made to discriminate different IWC levels by segregating the measurements by static air temperature (SAT), a common measurement available onboard commercial aircraft. The standard campaign sampling strategy [7] called for collecting measurement at four primary flight levels corresponding to temperatures of -20, -30, -40, and -50 degrees Celsius (±5 ºC). The resulting RRF associations with IWC in these 4 temperature intervals are shown in Figure 11.

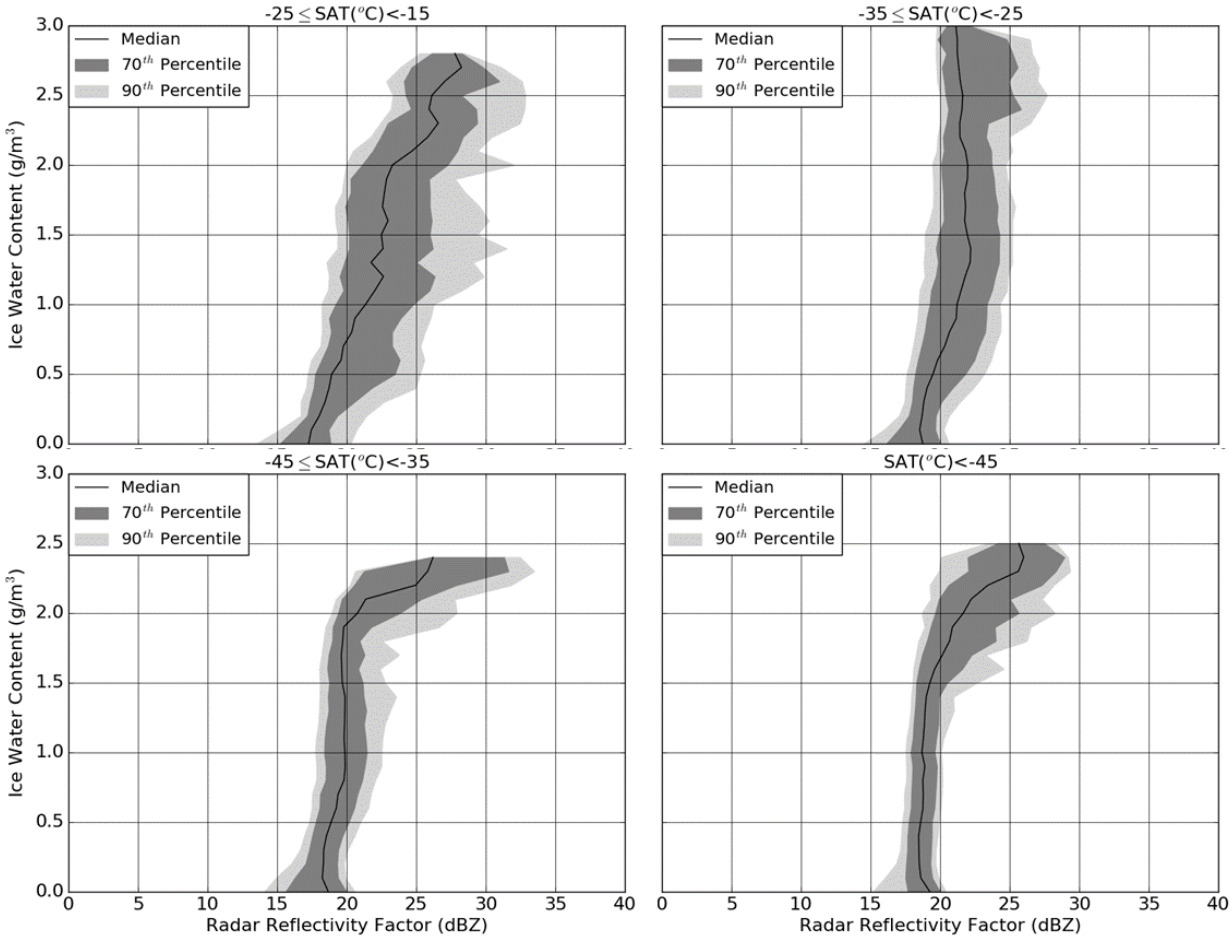

Figure 11: Relationship between X-Band RRF and IWC at Close Range Segregated by SAT. Data from 2015 & 2018 NASA HIWC Radar Flight Campaigns

Only the warmest temperature exhibits a possibly usable functional relationship with the median line, but the uncertainty in retrieved IWC is unacceptably large, as illustrated by the 70th percentile uncertainty. At all other temperatures the relationship remains mostly non-functional (i.e., vertical slope), with flat spots in the median comparison and an unacceptably large uncertainty envelope. It is worth noting that the large preponderance of measurements was collected at the -30 ºC flight level, consequently this temperature interval has a dominating impact on the overall results in Figure 10. This is also apparent in a statistical distribution of the RRF measurements (Figure 12) where measurements made with an SAT near -30 ºC are the largest contributor.

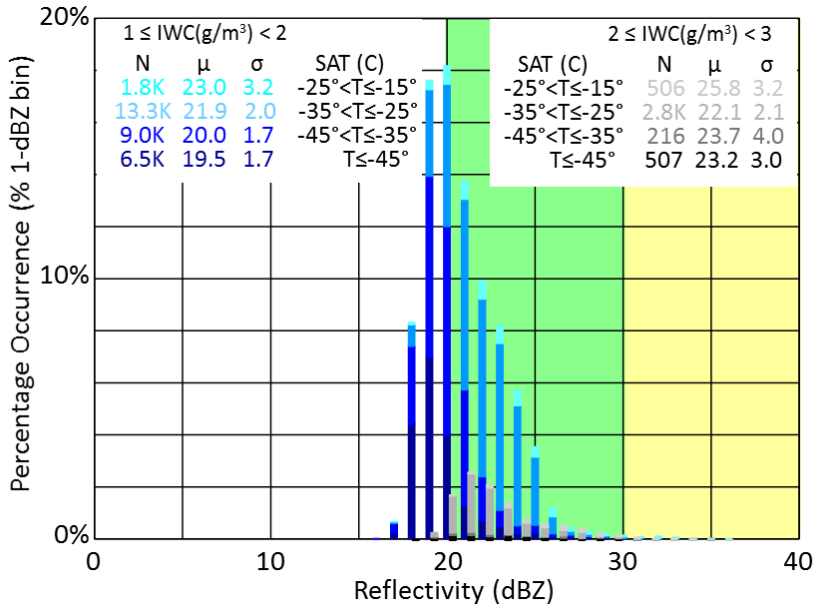

Figure 12: Statistical Distribution of X-Band RRF Measurements Associated with HIWC Conditions from all NASA Flights in 2015 and 2018 HIWC Radar Flight Campaigns. The typical range of green and yellow RRF for commercial weather radar are shaded as such on the plot itself.

With the RRF measurements grouped according to association with IWC defined here for discussion as moderate (1-2 g/m^3 – blue shades in Figure 12) or high (2-3 g/m^3 – gray shades in Figure 12), there is significant overlap between the distributions. The distribution associated with moderate IWC tends toward lower RRF at colder temperatures, but not enough to distinguish it from higher IWC. The temperature dependence for RRF measurements associated with high IWC is even less significant. These factors combine to make RRF by itself an unreliable discriminator of hazardous HIWC conditions.

- Assessment of Swerling Algorithm

Swerling algorithm comparisons were made in flight using research PPI images depicting RRF and RIWC overlaid with a line showing IWC measurements. The color-coded flight path represents IWC measured values (1 g/m^3 ≤ orange < 2 g/m^3 ≤ magenta). The data visualizations were shown only on research PPI displays and depict RRF and RIWC as shown in Figure 13. These research displays are used in post-flight analysis to visualize the spatially correlated remote and in-situ measurements for a given time.

Because the radar measures a volume of atmosphere ahead of the aircraft, radar measurements collected at multiple tilt angles were transformed into PPI displays at multiple altitudes. The PPI displays at the top in Figure 13 show enhanced RRF (left) and RIWC (right) at flight level and the two PPI displays on the bottom show the enhanced RRF (left) and the RIWC (right) at 5000 feet below flight level. Viewing enhanced RRF 5000 feet below flight level was used for situational awareness and maintaining safety – mission rules, as described in Ratvasky et al. [7], required the aircraft to maintain a 5000 foot (vertical) margin between the aircraft and overflight of any areas of high RRF (greater than 40 dBZ (red)). The research PPI displays were available in the cockpit via the onboard research network which allowed the pilots to make desired course changes to fly through HIWC regions detected ahead of the aircraft and avoid areas of high RRF.

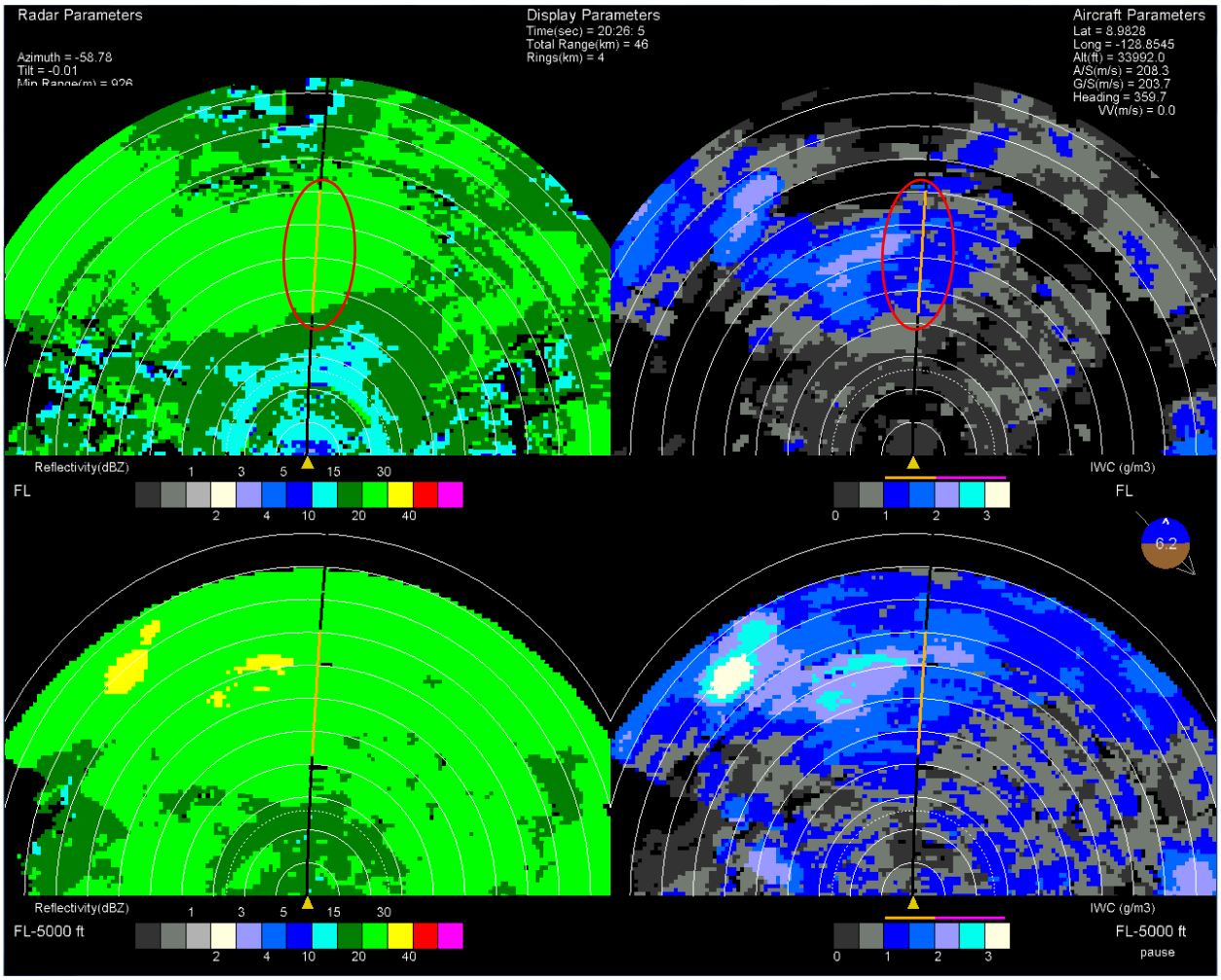

Figure 13: August 16 at 20:26:05 UTC. PPI displays of RRF (Left) and RIWC (Right) at flight level (Top) and at 5000 Feet <u>below</u> flight level (Bottom)

An example of the correlation between RIWC and IWC measured by the IKP2 from August 16th at 20:26:05 UTC is shown in Figure 13. The two PPI displays at flight level (Figure 13 top) show the flight path overlay in orange depicting IKP2 measured IWC levels of 1 to 2 g/m^3. The RIWC PPI display shows light and dark blues in this same area, indicating 1 to 1.5 g/m^3 and 1.5 to 2 g/m^3 respectively. On the corresponding enhanced RRF (left) PPI image, the same area is a solid green which represents RRF values between 20 to 30 dBZ. The area denoted in Figure 13 with red circles highlights the estimated RIWC for IWC level of 1 to 2 g/m^3 showing good correlation.

Another example of the correlation between RIWC and IWC but for higher IWC values (2 - 3 g/m^3) is shown in Figure 14. In this example, from 16 August 2018, the aircraft flew through a feeder band with a series of active cells associated with Tropical Storm Lane. The flight through the feeder band was conducted at an altitude of 30,000 feet and a temperature of -30 ^{o}C.

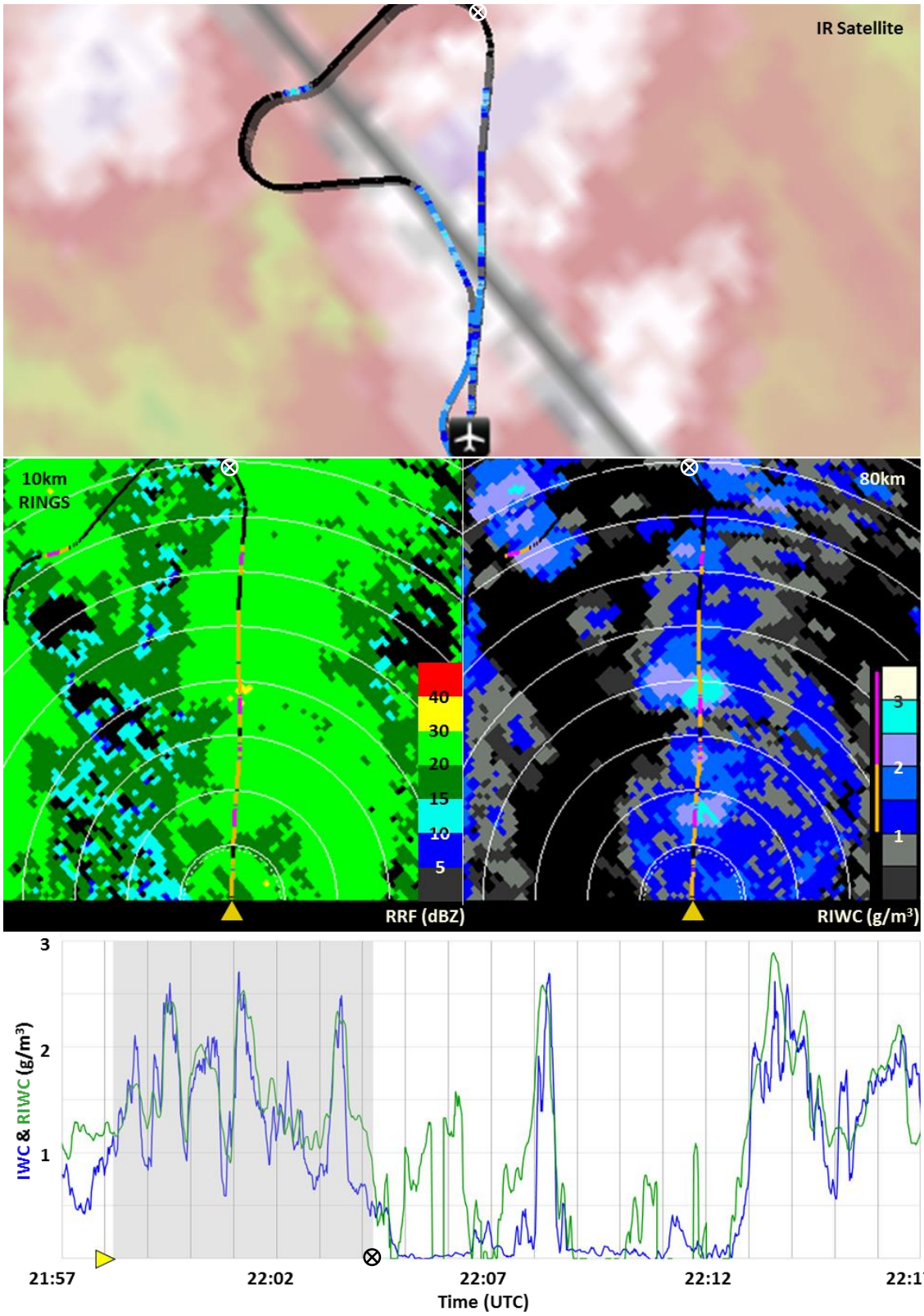

Figure 14: 16 August 2018, IR satellite image, enhanced RRF and RIWC with IWC overlay, and time history of RIWC and IWC (gray period in common with PPI displays).

Figure 14 shows the false color infrared brightness temperature satellite image [24] (top), the corresponding PPI images of RRF (left middle) and RIWC (right middle) at 21:58 UTC with a maximum range of 80 km (40 Nmi), and the time history comparison of RIWC and IKP2 IWC. The aircraft icon, on the satellite image, indicates the location of the aircraft at the time the radar images were captured. The two PPI images of RRF and RIWC are marked with a yellow triangle indicating this same aircraft location. The gray-shaded area, on the time plot, indicates the time segment corresponding to the flight path segment, beginning with the yellow triangle and ending at the ⊗, as shown on the three images.

The multicolored line overlaid on top of the PPI and satellite images is the aircraft flight path color coded to depict IKP2 measured IWC. The three magenta sections of the flight path correspond to the three IWC spikes in the time history plot between 21:58 to 22:04 UTC. At 21:58 UTC, the three spikes are about 14, 35, and 63 km from the aircraft. The enhanced RRF PPI image (Figure 14, left side) shows mostly 20 to 30 dBZ along the flight path associated with the first and third spikes at 14 and 63 km, respectively. The second spike at 35 km has RRF values of 30 to 40 dBZ. All three of these encounters produced IWC in excess of 2 g/m^3 without a commensurate increase or decrease in RRF. However, RIWC estimates associated with the three spikes produced 2.0 to 2.5 g/m^3 (purple) and 2.5 to 3.0 g/m^3 (cyan) consistently. The gray period of the time history plot shows peak IKP2 measured IWC values near 2.5 g/m^3; thus, RIWC estimates for all three spikes are within 0.5 g/m^3 of the IWC measured by the IKP2.

In addition to intensity comparisons, the size and location of the radar predicted HIWC regions compares favorably to IWC as measured by the IKP2. Using 2 g/m^3 to designate a HIWC region, there are three HIWC cells shown along the flight path in Figure 14. The first cell was encountered about 21:59:20 UTC (located ~14 km in the PPI image) and persisted for ~20 seconds; both the location and size (as predicted by the radar) are consistent with the measured IWC from the IKP2 as illustrated in the time history. The second cell was encountered at 22:01:00 UTC (located ~35 km in the PPI image) and persisted for ~20 seconds; again, these radar forecasts were consistent with the IKP2 observations. The third cell was encountered at 22:03:15 UTC (located ~63 km in the PPI image) and persisted for ~15 seconds; it too was consistent with the size and location as measured by the IKP2. Throughout the flight campaign, the radar predicted consistent regions of RIWC nine minutes or greater in advance of associated HIWC encounters as verified by in-situ measurements.

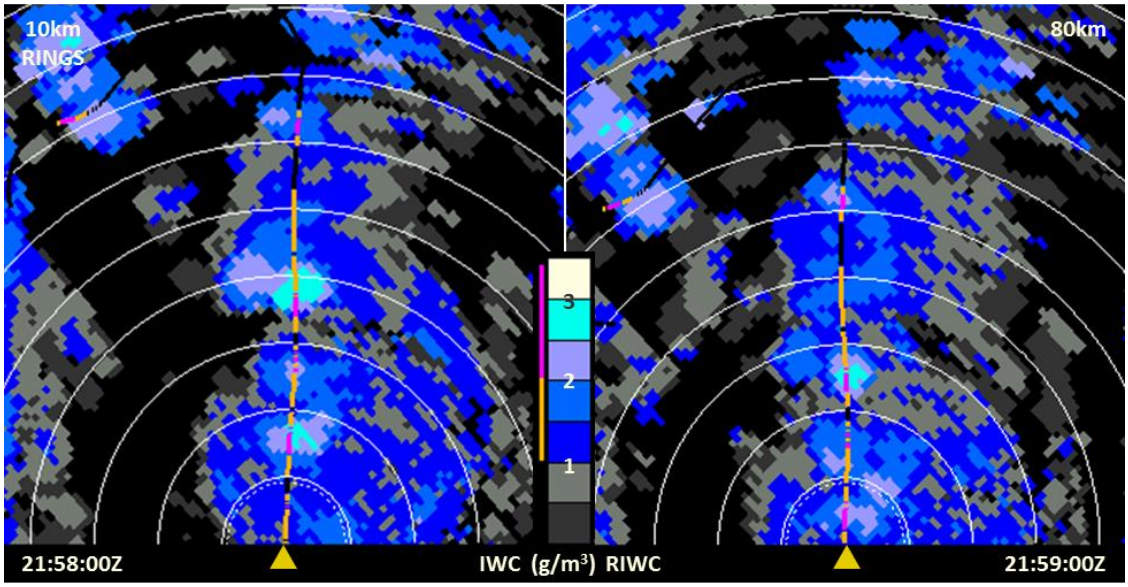

Figure 15: Consistency and persistence of RIWC measurements

RIWC estimates were observed to be consistent intensity and persistent from scan to scan throughout the flight campaign. Two RIWC PPI images from 16 August 2018 are shown in Figure 15, with range ring spacing of 10 km, and a maximum display range of 80 km (40 Nmi). In the left image are three IWC cells at 14, 35, and 63 km; in the right image these cells are now located at 2, 22, and 50 km from the aircraft. As shown in Figure 15, the cell closest to the aircraft decayed slightly and resulted in an RIWC estimate that agreed better with the in situ measured IWC. The second closest cell also slightly decayed and again resulted in better agreement with the in situ measured IWC. The third and smallest HIWC cell stayed the same throughout this encounter and also agreed with the in situ measured IWC. This example is typical of the persistent RIWC intensity, position, and extent estimates that are consistent with the IKP2 IWC measurements.

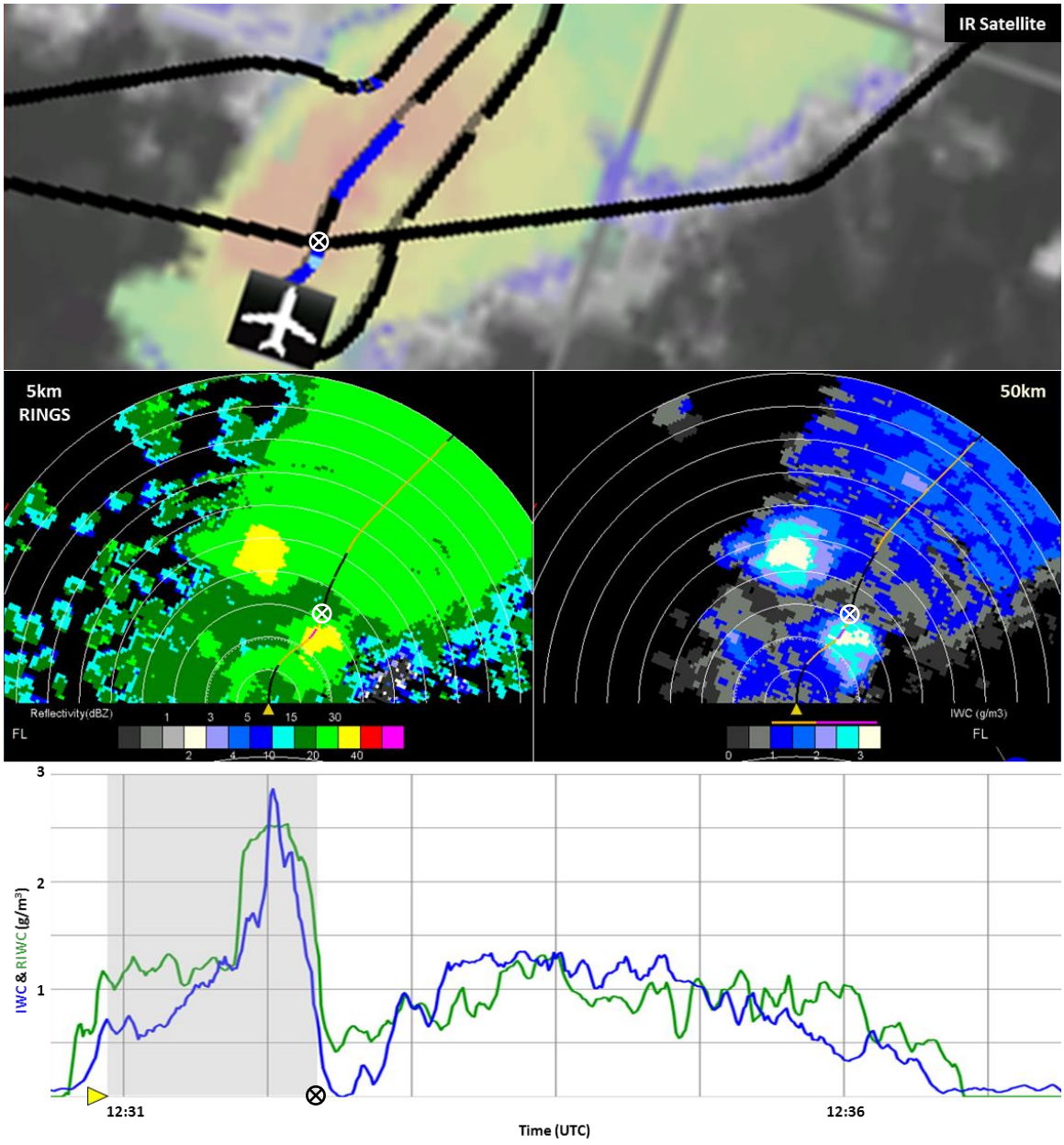

Figure 16: 06 August 2018 at 12:30 UTC. Satellite Image (Top), PPI Images of Enhanced RRF (Middle Left), RIWC (Middle Right) and Time History of RIWC and IWC from IKP2 (Bottom).

On August 6th, the DC-8 flew into deep convection occurring within the Gulf of Mexico. The storms were much smaller in scale than the systems encountered over the Pacific. The aircraft icon in the satellite image corresponds to the start of the time history plot (Figure 16, bottom) of IWC and RIWC. The two PPI displays shown in Figure 16 (middle) depict RRF (left) and RIWC (right) at flight level at 12:30 UTC. The aircraft flew at 32,000 feet and -37 ºC. As seen from both the time history plot and the PPI images the spatial positioning of IKP2 measured IWC and RIWC in these convective storms are positively correlated, similar to the examples above for Tropical Storm Lane. The time history plot shows a good estimate of RIWC relative to the IKP2 measured IWC, as they are typically within 0.5 g/m^3 and they peak at approximately the same value and location. The Gulf of Mexico and Hurricane Lane examples described above were flown at two different altitudes and temperatures. With good RIWC estimates for both flights, there are positive indications of consistent algorithm performance between the two temperatures of -30 ºC and -40 ºC.

The examples provided illustrate the performance of the RIWC algorithm. The Appendix contains RIWC PPI and RIWC-IKP2 time history comparisons for all flights of both campaigns, from which the overall algorithm performance can be viewed. Whereas in general the comparisons are quite favorable, there are periods in which the RIWC diverges from the IKP2, and these periods will provide important data for exploring algorithm improvement.

- Assessment of Turbulence

Spectral width estimates were made using pulse-pair signal processing and then associated with the RRF index of dispersion measurements used to make the RIWC estimates. This provided preliminary experimental results regarding the cross-coupling examined in the theoretical evaluation describe earlier. In all of the observed HIWC conditions, the spectral width estimates at close range were significantly less than the Nyquist velocity (Figure 17).

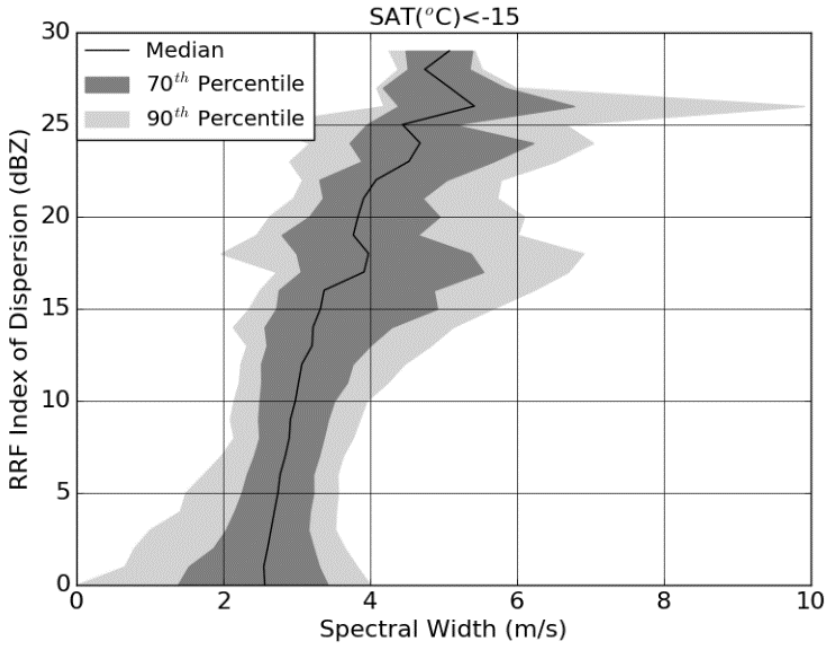

Figure 17: Experimental Impact of Estimated Spectral Width on Measured RRF Index of Dispersion.

As predicted by the theoretical evaluation – when spectral width is much less than the Nyquist velocity – the RRF index of dispersion measurements exhibit very little relation to the spectral width estimates and are instead dominated by the variances in the signal amplitude. Furthermore, the spectral width estimates may not be an accurate measure of the frequency variances (i.e. resulting from atmospheric turbulence), but rather the result of cross-coupling from the large signal amplitude variances. Associating these estimates with actual turbulence measurements will provide insight into the practical implications of the theoretical relationship (see Future Work).

Summary/Conclusions

Analysis of the radar measurements collected during the HIWC RADAR Flight Campaigns confirmed previous findings that current airborne weather radars do not detect hazardous high ice water content associated with low reflectivity. These conditions have caused engine power loss and damage events and air data probe anomalies. Attempts to detect HIWC conditions using RRF in conjunction with other measurements such as SAT show that RRF is insufficient. This is due to the particular nature of HIWC PSDs, with high concentrations of very small ice particles that have less impact on RRF measurements relative to their mass than larger particles. Without an estimate of the PSD, it is not possible to accurately determine IWC using RRF in HIWC conditions.

Multi-Frequency and Polarimetric enhancements to radars have been shown by others to have some potential to improve measurement of HIWC conditions. However, no commercial radar products have yet been developed and deployed. Additionally, airframe and airline personnel have expressed concerns of potentially increased system/maintenance costs and operational/re-certification complexities. Consequently, there is considerable industry reluctance to consider significant modifications to the existing radar technology for HIWC detection and avoidance. This was an important factor considered by NASA radar engineers when exploring new HIWC detection and avoidance algorithms.

NASA and the FAA have conducted two flight campaigns with the NASA DC-8 to study the potential for improving weather radar detection of HIWC conditions. In both flight campaigns, the DC-8 was instrumented with a commercial, X-band, aircraft, weather radar modified to transfer radar return signals to a data recorder and a research processing system. The aircraft was also equipped with a suite of cloud in-situ probes for directly measuring the conditions. A correlation between IWC and the variability in radar reflectivity measurements– represented by the RRF index of dispersion – was identified during analysis of the measurements collected during the 2015 HIWC RADAR I Flight Campaign. This led to a simple technique for remotely estimating IWC with such a commercial weather radar. The resulting experimental RIWC algorithm was implemented in research radar processing systems and operated during the 2018 HIWC RADAR II Flight Campaign. It provided real-time predictions of regions containing HIWC conditions ahead of the aircraft, which were confirmed shortly afterwards by directly sampling those regions with the cloud in-situ probes.

The new NASA RIWC algorithm was observed to provide consistent and encouragingly accurate estimates of IWC out to 60 nautical miles for IWC conditions ranging from less than 0.5 g/m^3 to more than 3.0 g/m^3. The estimate was typically within about ± 0.5 g/m^3 of the IKP measurement. The 60 nautical mile limit was only due to measurement limitation and not due to radar sensitivity or algorithm performance. The examples presented in this paper were chosen to demonstrate specific aspects of the algorithm and its performance. The PPI imagery was captured at a nominal 40 nautical mile range; which was also not indicative of any limitation of the algorithm's function. The only theoretical range limit to the Swerling RIWC algorithm is the inherent SNR requirement to make a valid measurement and the geometric limit due to the ever-increasing pulse volume that will eventually encompass ground clutter and lower altitude weather conditions significantly different from those at flight level.

Preliminary analysis of RIWC estimates using this technique show little to no range degradation within the 60 nautical miles. The NASA algorithm functions using current waveforms and current hardware, only requiring the addition of a single calculation in order to provide long-range HIWC detection and avoidance information. Therefore, this capability for RIWC can be implemented on current radars by means of software upgrades. The NASA RIWC algorithm has been offered as the basis for minimum operational performance standards now being developed within an RTCA Special Committee (SC-230) Working Group (WG-10).

Future Work

Performance analysis of the RIWC algorithm will continue with a focus on more quantitative assessments. A final determination of the algorithm's effectiveness cannot be completed until the detection requirements are defined. However, evaluation criteria being considered include median RIWC correlations to IWC with percentile contours, RIWC estimates with specified confidence levels, statistical probabilities based on a fixed IWC threshold, and statistical representations of RIWC correlations to IWC given multiple or variable thresholds. For the statistical assessments, the confusion matrix will be considered to quantify HIWC detections (true positive), HIWC rejections (true negative), nuisance alarms (false positive), and missed detections (false negative).

Modeling and simulation efforts have been started to build upon the theoretical evaluation summarized above. These will focus on evaluating the RIWC algorithm performance under simulated flight conditions including HIWC and others not encountered during either flight campaign. The controlled nature of the simulations will help identify how the RIWC algorithm responds to specific HIWC conditions and non-HIWC rain and turbulent conditions. This will also support possible future certification efforts.

In addition to the theoretical evaluation and planned simulation effort, an assessment of the impact of turbulence on the RIWC algorithm is being performed using data from the flight campaigns. Specifically, the radar measured spectral width – which provides a remote estimate of turbulence – and the accelerations measured onboard the aircraft – which are a measure of the turbulence experienced – can be correlated with the RIWC estimates. The purpose is to ensure that turbulence does not result in false HIWC indications.

While RIWC results were computed and displayed in real-time during the flight campaign, it was on experimental research displays only and not intended to replace the standard cockpit display. Potential future implementations for commercial applications will require addressing human-machine interface (HMI) considerations.

RTCA SC-230 WG-10 has initiated development of Minimum Operational Performance Standards (MOPS) for radar detection of HIWC conditions. Data from the flight campaign and the current study will provide critical information to this group. The MOPS will define what constitutes a hazard and the requirements for detecting and displaying information to the crew.

References

1.Mason, J., Strapp, J.W., Chow, P., "The Ice Particle Threat to Engines in Flight," AIAA 2006-0206, https://doi.org/10.2514/6.2006-206

2.Mason, J., Grzych, M., "The Challenges Identifying Weather Associated With Jet Engine Ice Crystal Icing", SAE Technical Paper, 2011-38-0094, 2011, https://doi.org/10.4271/2011-38-0094

3.Strapp, J. W., G. A. Isaac. A. Korolev, T. Ratvasky, et al., "The High Ice Water Content (HIWC) Study of deep convective clouds: Science and technical plan.",2016, FAA Rep. DOT/FAA/TC-14/31, available at http://www.tc.faa.gov/its/worldpac/techrpt/tc14-31.pdf. 105 pps.

4.Title 14 Code of Federal Regulations, Part 25 and 33 Appendix D. Airplane and Engine Certification Requirements in Supercooled Large Drop, Mixed Phase, and Ice Crystal Icing Conditions. Docket No. FAA–2010–0636; Amendment Nos. 25–140 and 33–34, published by the Office of the Federal Register, National Archives and Records Administration, Washington, DC. Effective November 4, 2014.

5.EASA CS 25 Book 1 Appendix P, annex to Executive Director Decision 2015/008/R of 12 March 2015 amending Certification Specifications and Acceptable Means of Compliance for Large Aeroplanes CS-25 at Amendment 16. Available from https://www.easa.europa.eu/document-library/certification-specifications/cs-25-amendment-16.

6.Dezitter, F., A. Grandin, J.-L. Brenguier, F. Hervy, H., et al., "HAIC - High Altitude Ice Crystals," 5th AIAA Atmospheric and Space Environments Conference, American Institute of Aeronautics and Astronautics http://arc.aiaa.org/doi/abs/10.2514/6.2013-2674

7.Ratvasky, T., Harrah, S., Strapp, J.W., Proctor, F., et al., "Summary of the High Ice Water Content (HIWC) Radar Flight Campaigns", SAE Technical Paper,2019-01-2027, 2019.

8.Sassen, Kenneth, "Ice Cloud Content from Radar Reflectivity." Journal of Climate and Applied Meteorology, 26, 1050-1053. 2 August 1986 and 28 February 1987, https://doi.org/10.1175/1520-0450(1987)026<1050:ICCFRR>2.0.CO;2

9.Pokharel, Binod andVali Gabor, "Evaluation of Collocated Measurements of Radar Reflectivity and Particle Sizes in Ice Clouds." Journal of Climate and Applied Meteorology, 50, 2104-2119. 21 April 2011, https://doi.org/10.1175/JAMC-D-10-05010.1

10. Hogan, R. J., Mittermaier M. P., and Illingworth, A.J., "The Retrieval of Ice Water Content from Radar Reflectivity Factor and Temperature and Its Use in Evaluating a Mesoscale Model, Journal of Applied Meteorology and Climatology, Vol. 45(2), February 2006, pp. 301–317, https://doi.org/10.1175/JAM2340.1

11. Hong, G., Yang, P., Baum, B.A., Heymsfield, A.J., "Relationship between ice water content and equivalent radar reflectivity for clouds consisting of nonspherical ice particles," Journal of Geophysical Research, 113, D20205. 12 October 2008, https://doi.org/10.1029/2008JD009890

12. Heymsfield, A.J., Wang, Z., Matrosov, S., "Improved Radar Ice Water Content Retrieval Algorithms Using Coincident Microphysical and Radar Measurements," Journal of Applied Meteorology, Vol. 44(9), September 2005, pp. 1391–1412. https://doi.org/10.1175/JAM2282.1

13. Doviak, Richard J. and Zrnic, Dusan S., Doppler Radar and Weather Observations. Academic Press, Inc., 1984.

14. Locatelli, J. D. and Hobbs, P. V., "Fall Speeds and Masses of Solid Precipitation Particles." Journal of Geophysical Research, 79, 2185-2197. 20 May 1974, https://doi.org/10.1029/JC079i015p02185

15. Smith, P. L., "Equivalent Radar Reflectivity Factors for Snow and Ice Particles." Journal of Climate and Applied Meteorology, 23, 1258-1260. 28 November 1983 and 2 May 1984, https://doi.org/10.1175/1520-0450(1984)023%3C1258:ERRFFS%3E2.0.CO;2

16. Marshall, J. S. and Palmer, W. McK., "The Distribution of Raindrops with Size." Journal of Meteorology, 5, 165-166. 26 January 1948, https://doi.org/10.1175/1520-0469(1948)005%3C0165:TDORWS%3E2.0.CO;2

17. Marshall, J. S. and Gunn, K.L.S., “Measurement of Snow Parameters by Radar.” Journal of Meteorology, 9, 322-327. 3 June 1952, https://doi.org/10.1175/1520-0469(1952)009<0322:MOSPBR>2.0.CO;2

18. Pazmany, A. L., “Investigation of Advanced Radar Techniques for Atmospheric Hazard Detection with Airborne Weather Radar,” August, 2014. NASA/CR–2014-218510. https://ntrs.nasa.gov/archive/nasa/casi.ntrs.nasa.gov/20150000582.pdf

19. Sekelsky, S. M., Ecklund, W. L., Firda, J. M., Gage, K. S., KcIntosh, R. E., “Particle Size Estimation in Ice-Phase Clouds Using Multifrequency Radar Reflectivity Measurements at 95, 33, and 2.8 GHz.” Journal of American Meteorological Society, 1999, 5-28. 20 April 1998, https://doi.org/10.1175/1520-0450(1999)038%3C0005:PSEIIP%3E2.0.CO;2

20. Nguyen, C. M., Wolde, M., and Korolev, A., “Determination of Ice Water Content (IWC) in tropical convective clouds from X-band dual-polarization airborne radar,” Atmos. Meas. Tech. Discuss., https://doi.org/10.5194/amt-2019-62, in review, 2019

21. Swerling, Peter (April 1960). "Probability of Detection for Fluctuating Targets". IRE Transactions on Information Theory. 6 (2): 269–308. Originally published 17 March 1954 as RAND Research Memorandum RM-1217, https://doi.org/10.1109/TIT.1960.1057561

22. Strapp, J.W., Lilie, L., Ratvasky, T., Davison, C., et al, “Isokinetic TWC Evaporator Probe: Development of the IKP2 and Performance Testing for the HAIC-HIWC Darwin 2014 and Cayenne Field Campaigns,” AIAA 2016-4059, 2016, http://dx.doi.org/10.2514/6.2016-4059

23. Davidson, C., Strapp, J.W., Lilie, L., Ratvasky, T., et al, “Isokinetic TWC Evaporator Probe: Calculations and Systemic Uncertainty Analysis,” AIAA 2016-4060, 2016, http://dx.doi.org/10.2514/6.2016-4060

24. Bedka, K., Yost, C., Nguyen, L., Strapp, J. et al., "Analysis and Automated Detection of Ice Crystal Icing Conditions Using Geostationary Satellite Datasets and In Situ Ice Water Content Measurements," SAE Technical Paper 2019-01-1953, 2019, https://doi.org/10.4271/2019-01-1953

Acknowledgments

Many people contributed to the success of these flight campaigns and the development of the RIWC algorithm. The authors are grateful to all who helped and want to specifically recognize:

- Tom Bond (FAA Chief Scientific and Technical Advisor for Flight Environmental Icing) for his tireless support and encouragement developing icing sciences and mitigation technologies.
- Lee Nguyen (FAA AIR-6B0) for his lengthy support for developing new radar products and their certification standards.
- James Riley and Stephanie DiVito for their sustained financial and technical support without whom these flight campaigns could not have been conducted.

Special recognition is made to the NASA DC-8 team, particularly:

- Adam Webster, Dave Van Gilst, and Sebastian Rainer for their help integrating the research systems with the DC-8 and making everything work together;
- Tim Moes, Matt Berry, Ken Norlin, Brennan Wehr, Dave Fedors, Frank Batteas, Wayne Ringelberg, and Nils Larsen for conducting safe flight operation;
- Louis Nguyen, Kris Bedka, and Chris Yost from NASA Langley, Matt Grzych from Boeing, and Ben Bernstein from Leading Edge Atmospherics for their forecast support;
- Dave Vicanti, Bob Jensen, and Paul Christianson from Honeywell Aerospace for their collaboration and technical services.

Thanks also are extended to:

- NCAR’s Julie Haggerty for data archive and instrumentation support.
- Retired Boeing engineer Jeanne Mason who challenged us to explain what was

happening in the atmosphere to cause these issues; then pressed us to develop a means to detect and discriminate hazardous IWC from benign conditions; and who always expressed faith that we could achieve all our goals if we just kept at it.

This research and development was sponsored by NASA's Advance Air Vehicles Program through the Advance Air Transport Technology (AATT) and the Aeroscience Evaluation Test Capabilities (AETC) projects and by the FAA's Aviation Weather Research Program.

Definitions/Abbreviations

AFRC	Armstrong Flight Research Center
CDP-2	Cloud Droplet Probe (DMT)
COTS	Commercial Off The Shelf
CPI	Coherent Processing Interval
dB	Decibels
^{o}C	Degrees Celsius
DMT	Droplet Measurement Technologies
FAA	Federal Aviation Administration
FFT	Fast Fourier Transform
GRC	Glenn Research Center
HAIC	High Altitude Ice Crystal
HIWC	High Ice Water Content
HMI	Human-Machine Interface
I&Q	In-phase and Quadrature
I_D	Index of Dispersion
IWC	Ice Water Content
K_{DP}	Specific Differential Phase
KFLL	Fort Lauderdale/Hollywood International Airport
KPMD	Palmdale Regional Airport
LaRC	Langley Research Center
L_{DR}	Linear Depolarization Ratio
MCS	Mesoscale Convective System
MEL	Minimum Equipment List
MFD	Multi-Function Display
MOPS	Minimum Operational Performance Standards
NASA	National Aeronautics and Space Administration
Nmi	Nautical Miles
NRCC	National Research Council Canada
PHKO	Kona International Airport
PIP	Precipitation Imaging Probe (DMT)
PPI	Plan Position Indicator
PRF	Pulse Repetition Frequency
PRI	Pulse Repetition Interval
PSD	Particle Size Distribution
QA	Quality Assurance
RCS	Radar Cross Section

RF	Radio Frequency
RIWC	Radar Ice Water Content
RRF	Radar Reflectivity Factor
RTCA	Radio Technical Commission for Aeronautics
SAT	Static Air Temperature
SC	Special Committee
SEA	Science Engineering Associates
SNR	Signal to Noise Ratio
TAT	Total Air Temperature
TWC	Total Water Content
UTC	Coordinated Universal Time
WG	Working Group
Z_{DR}	Polarimetric Differential Reflectivity

Appendix

The following images illustrate the RIWC estimates observed during the HIWC Radar Flight Campaign(s). They were produced as a mosaic of individual airborne weather radar scans collected throughout the day. All scans were at zero tilt and represent the RIWC observed at flight level. Individual scans are nominally 60 nautical miles in range and ± 60° in azimuth (referenced to the aircraft body axis and/or heading). The flight path is also illustrated indicating where the aircraft flew. The images show remote RIWC estimates away from the flight path which consequently were never sampled by the in-situ instruments.

Each image is accompanied by a time history of RIWC estimates associated with IWC measurements made by the IKP2. Only the subset of RIWC estimates made at locations along the flight path can be associated with in-situ measurements. These use radar measurements made at the closest range directly in front of the aircraft, which are believed to produce the best spatial resolution, highest SNR, and least time elapsed between the radar measurement and IKP2 measurement.

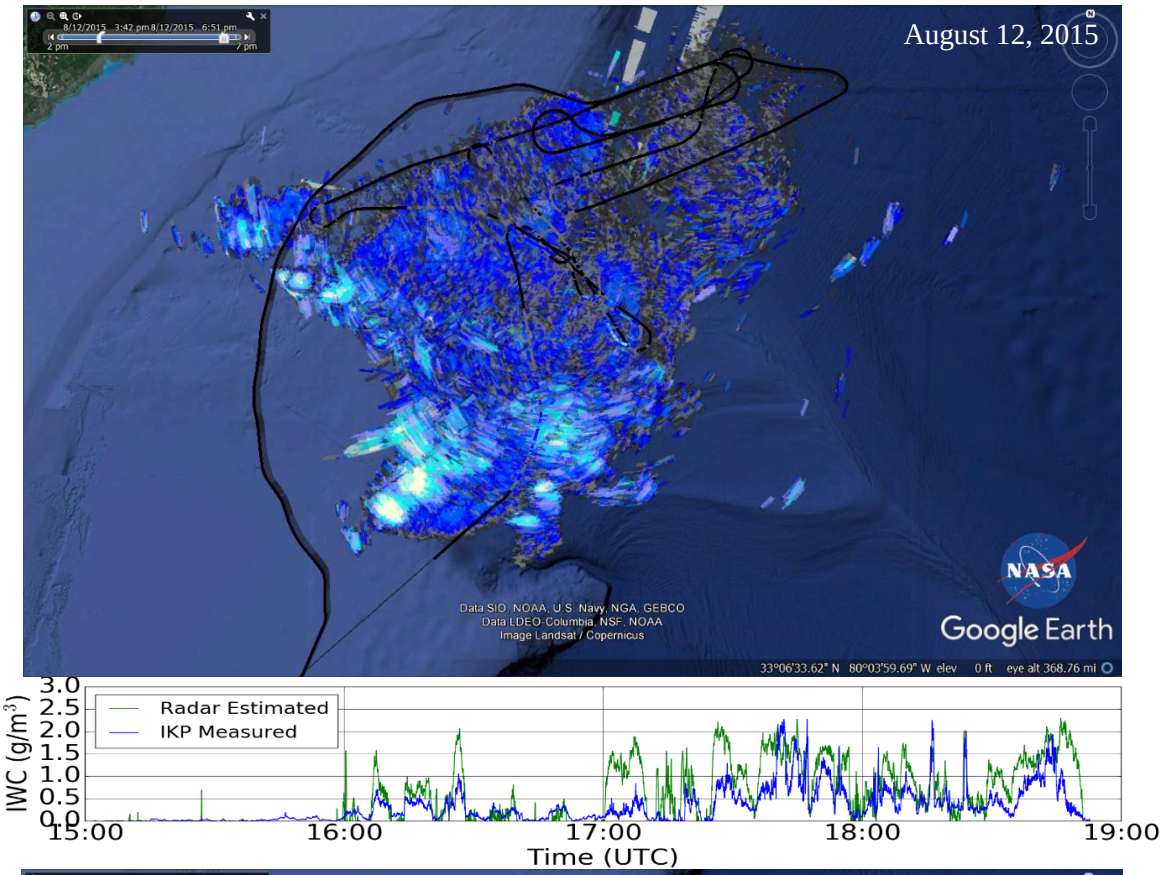
August 12, 2015
Data SIO, NOAA, U.S. Navy, NGA, GEBCO
Data LDEO-Columbia, NSF, NOAA
Image Landsat / Copernicus
Google Earth
33°06'33.62" N 80°03'59.69" W elev 0 ft eye alt 368.76 mi
Radar Estimated
IKP Measured
IWC (g/m³)
3.0
2.5
2.0
1.5
1.0
0.5
0.0
15:00
16:00
17:00
18:00
19:00
Time (UTC)

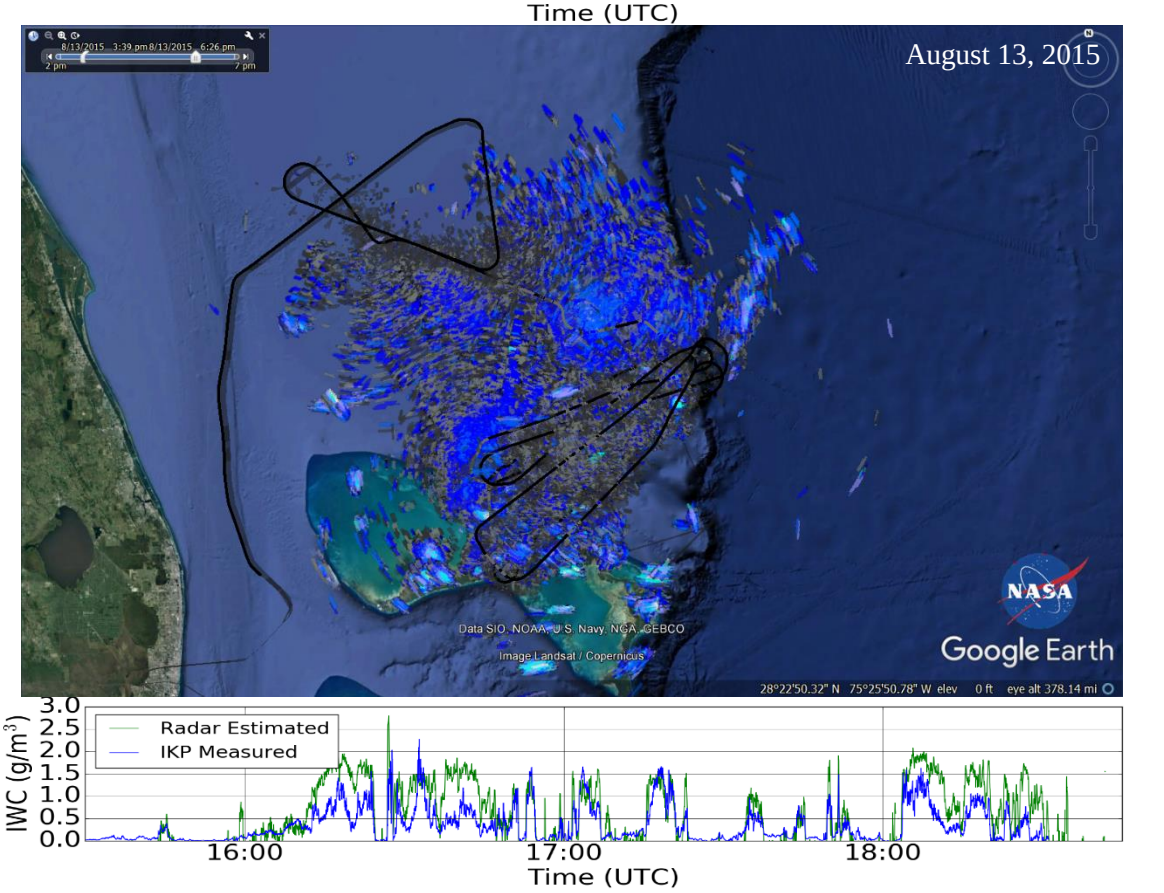
August 13, 2015
Data SIO, NOAA, U.S. Navy, NGA, GEBCO
Image Landsat / Copernicus
Google Earth
28°22'50.32" N 75°25'50.78" W elev 0 ft eye alt 378.14 mi
Radar Estimated
IKP Measured
IWC (g/m³)
3.0
2.5
2.0
1.5
1.0
0.5
0.0
16:00
17:00
18:00
Time (UTC)

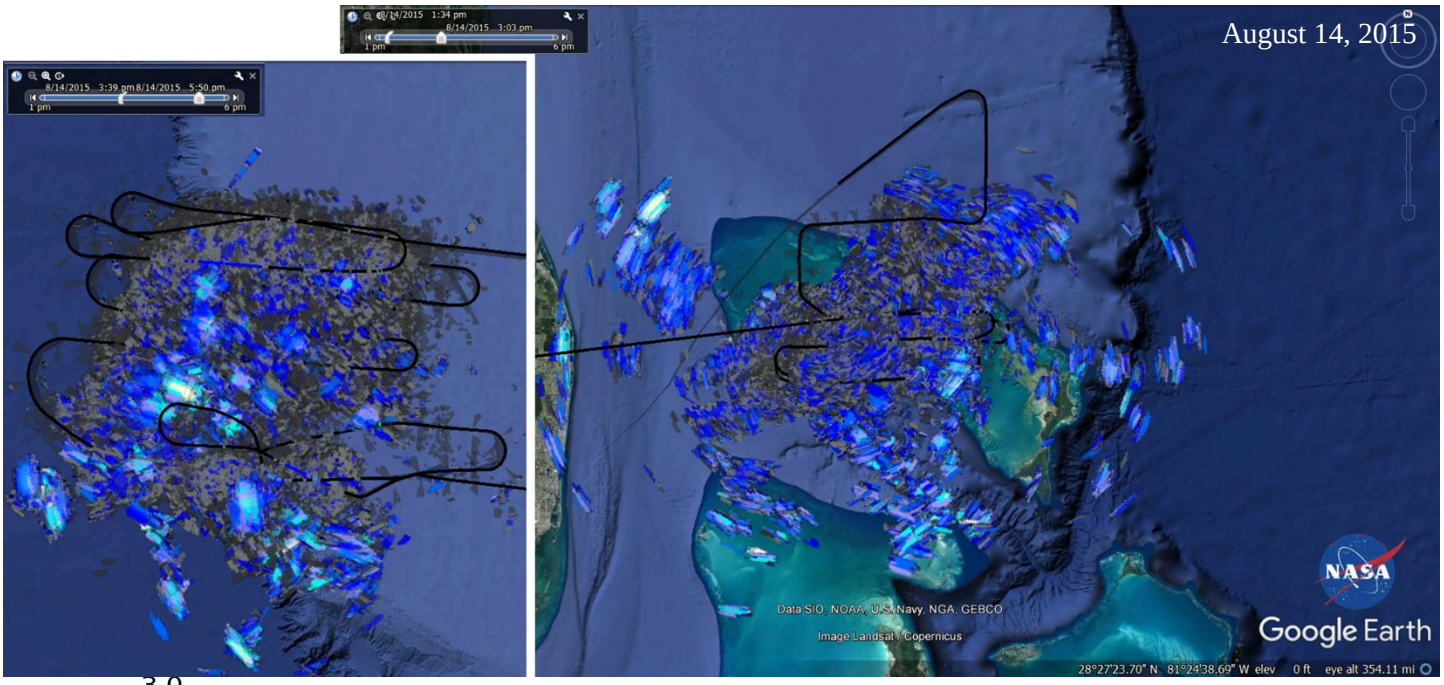
August 14, 2015
Data SIO, NOAA, U.S. Navy, NGA, GEBCO
Image Landsat / Copernicus
Google Earth

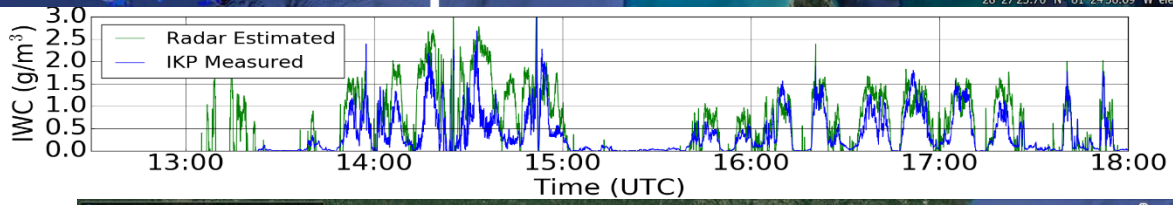
Radar Estimated
IKP Measured
IWC (g/m³)
3.0
2.5
2.0
1.5
1.0
0.5
0.0
13:00
14:00
15:00
16:00
17:00
18:00
Time (UTC)

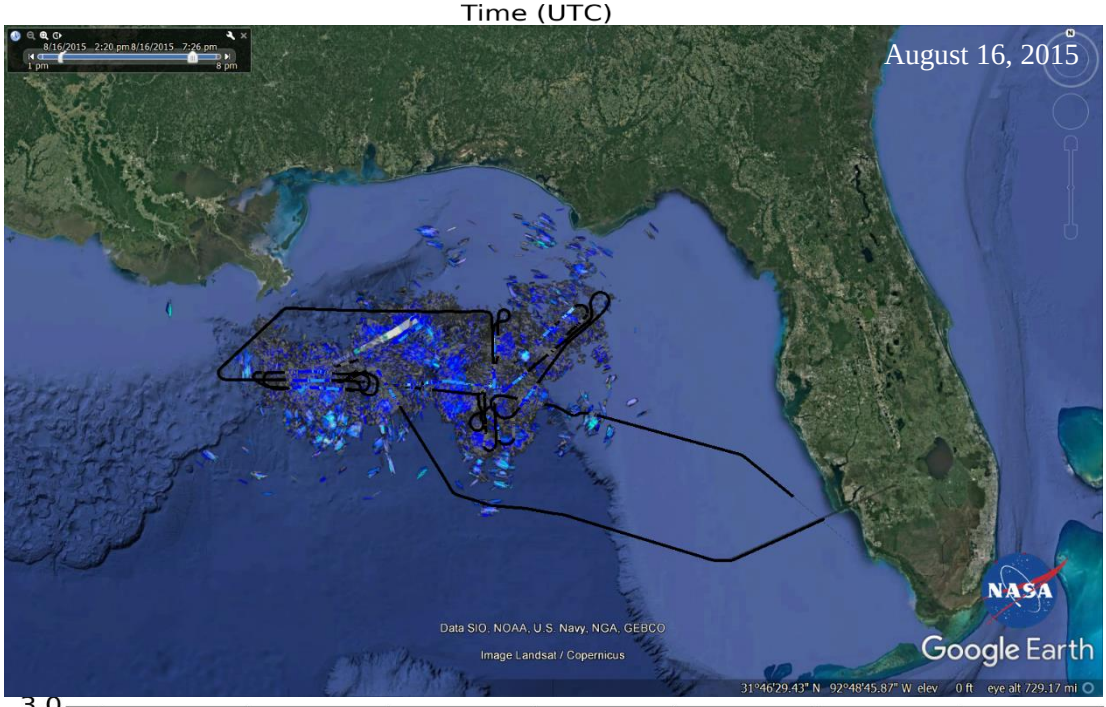
August 16, 2015
Data SIO, NOAA, U.S. Navy, NGA, GEBCO
Image Landsat / Copernicus
Google Earth

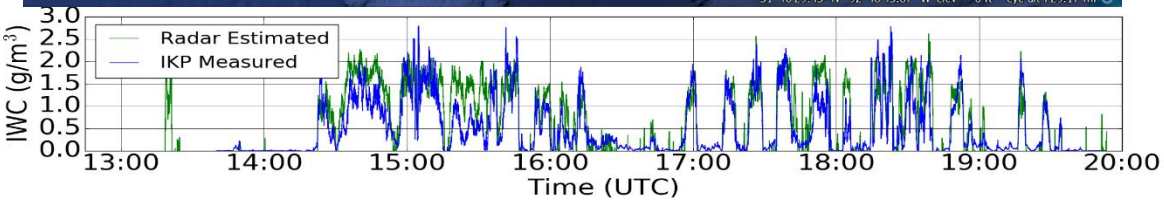
Radar Estimated
IKP Measured
IWC (g/m³)
3.0
2.5
2.0
1.5
1.0
0.5
0.0
13:00
14:00
15:00
16:00
17:00
18:00
19:00
20:00
Time (UTC)

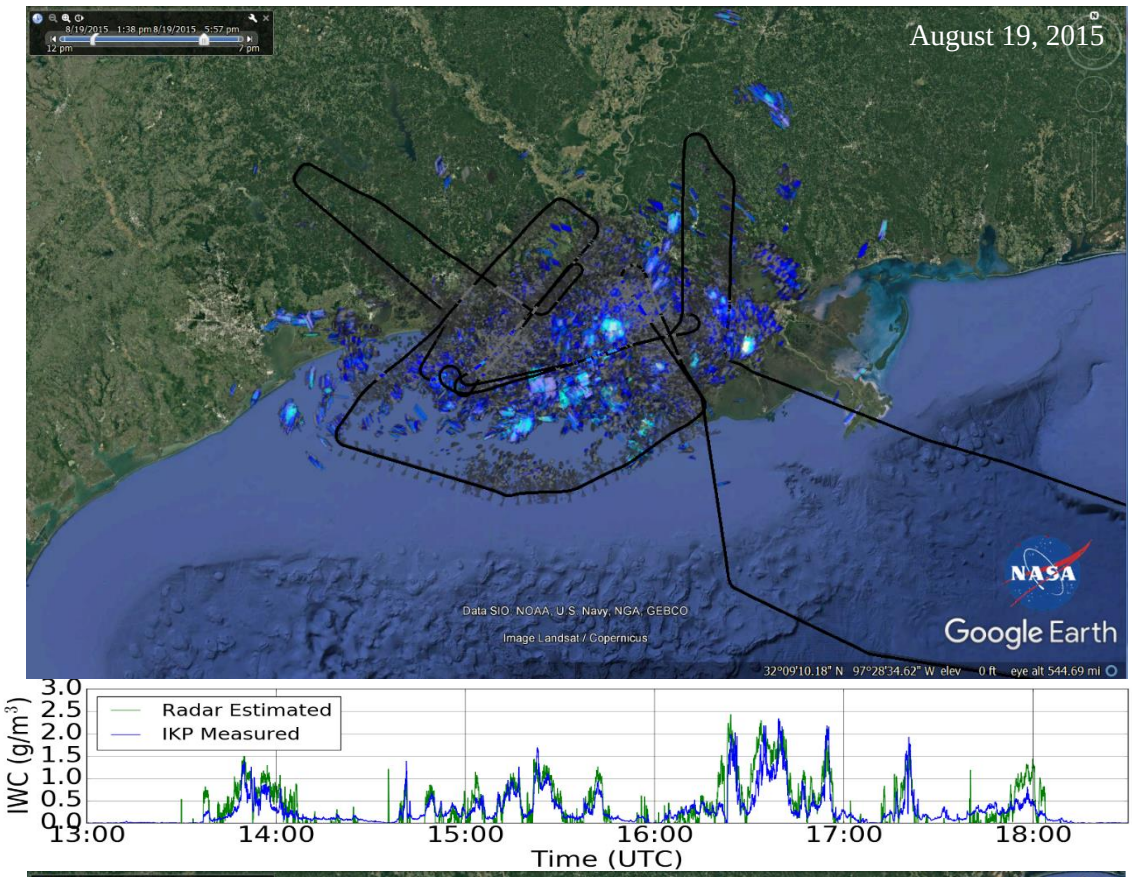
August 19, 2015
Data SIO, NOAA, U.S. Navy, NGA, GEBCO
Image Landsat / Copernicus
Google Earth
32°09'10.18" N 97°28'34.62" W elev 0 ft eye alt 544.69 mi
Radar Estimated
IKP Measured
IWC (g/m³)
3.0
2.5
2.0
1.5
1.0
0.5
0.0
13:00
14:00
15:00
16:00
17:00
18:00
Time (UTC)

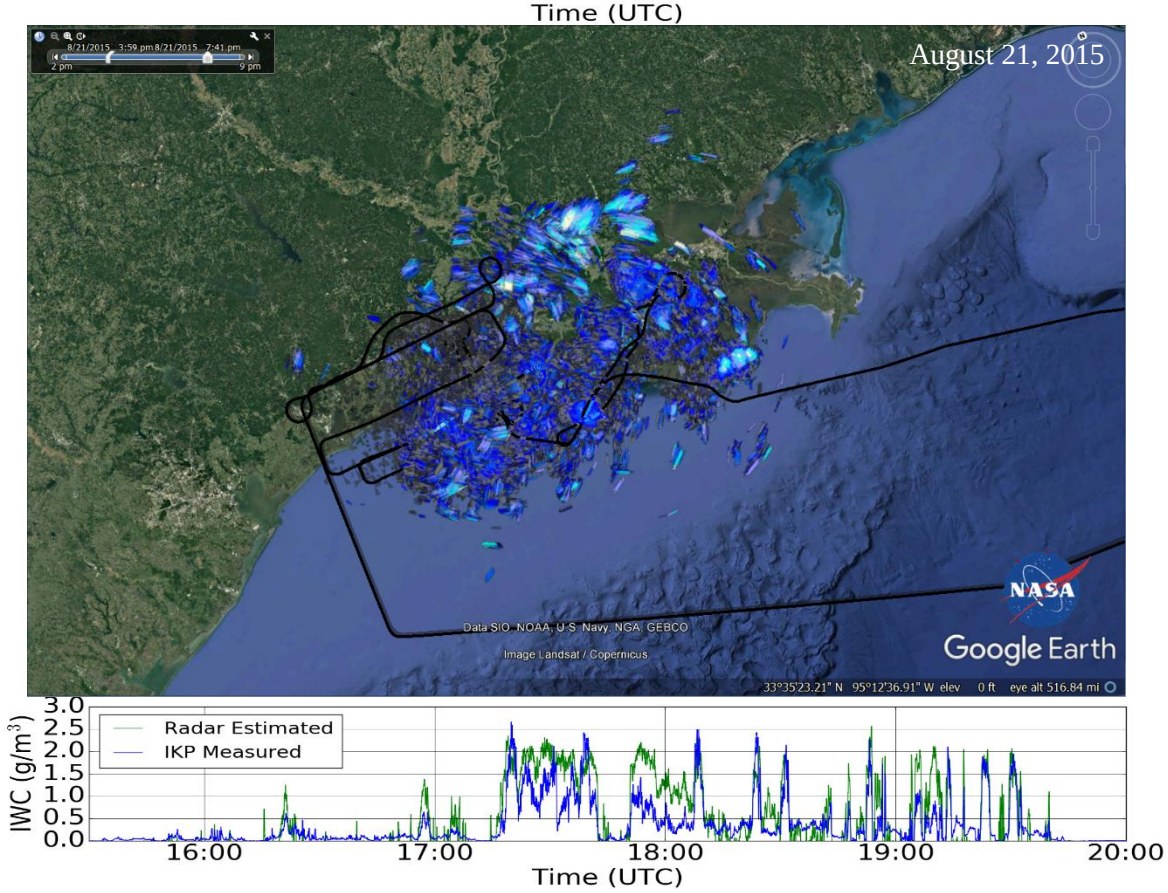
August 21, 2015
Data SIO, NOAA, U.S. Navy, NGA, GEBCO
Image Landsat / Copernicus
Google Earth
33°35'23.21" N 95°12'36.91" W elev 0 ft eye alt 516.84 mi
Radar Estimated
IKP Measured
IWC (g/m³)
3.0
2.5
2.0
1.5
1.0
0.5
0.0
16:00
17:00
18:00
19:00
20:00
Time (UTC)

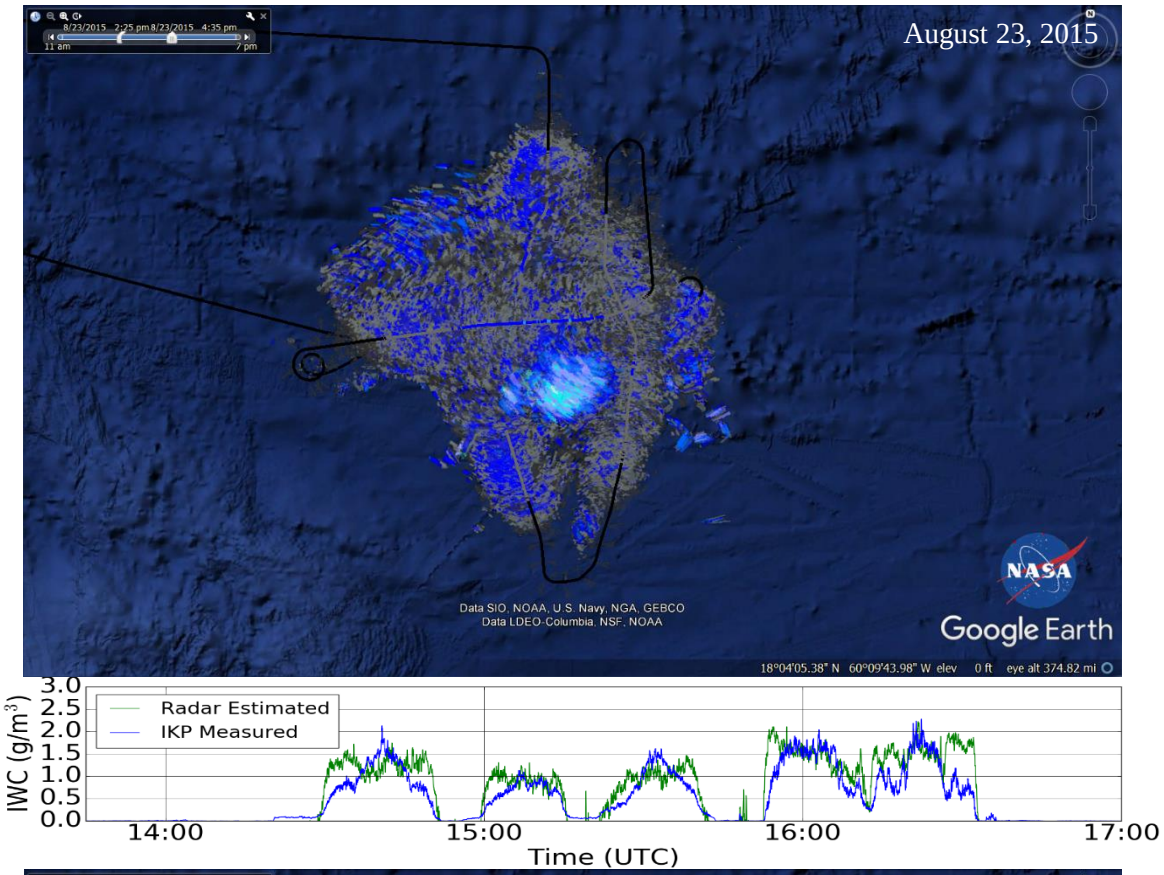
August 23, 2015
Data SIO, NOAA, U.S. Navy, NGA, GEBCO
Data LDEO-Columbia, NSF, NOAA
Google Earth
Radar Estimated
IKP Measured
IWC (g/m³)
Time (UTC)
14:00
15:00
16:00
17:00

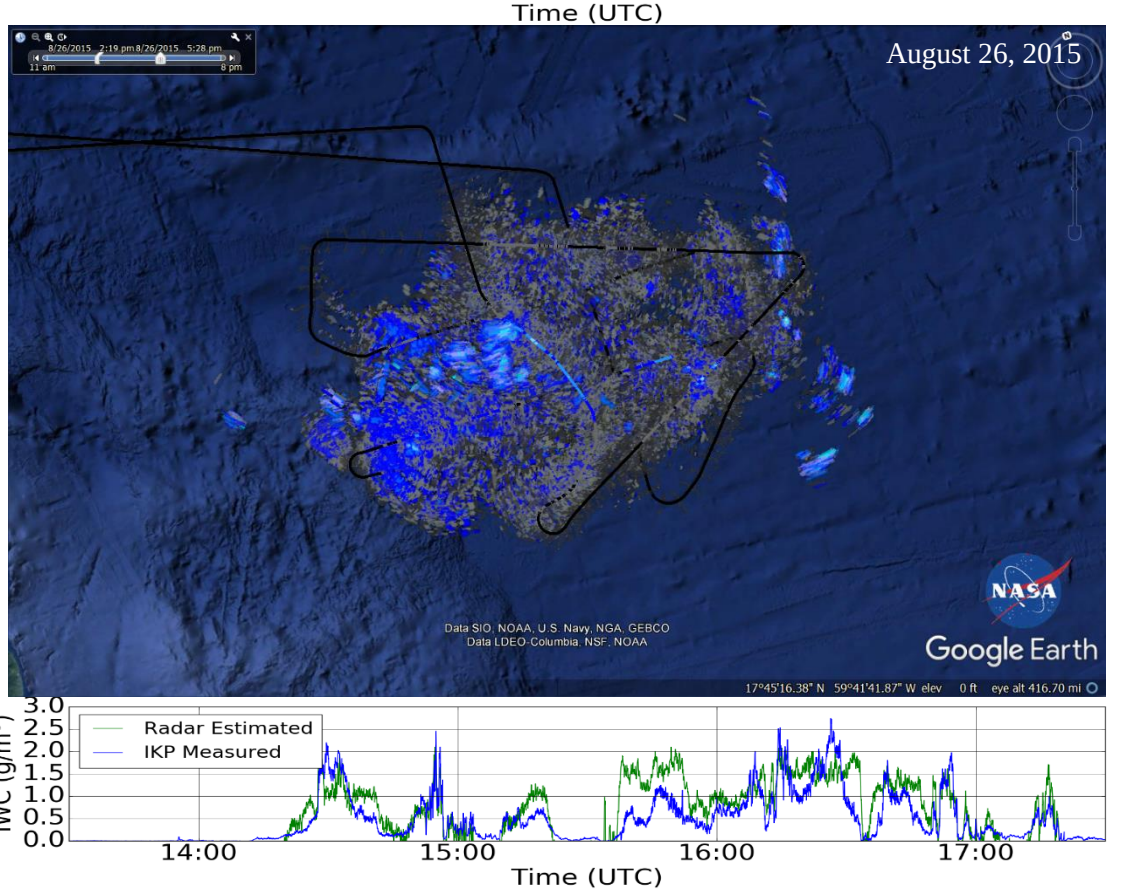
August 26, 2015
Data SIO, NOAA, U.S. Navy, NGA, GEBCO
Data LDEO-Columbia, NSF, NOAA
Google Earth
Radar Estimated
IKP Measured
IWC (g/m³)
Time (UTC)
14:00
15:00
16:00
17:00

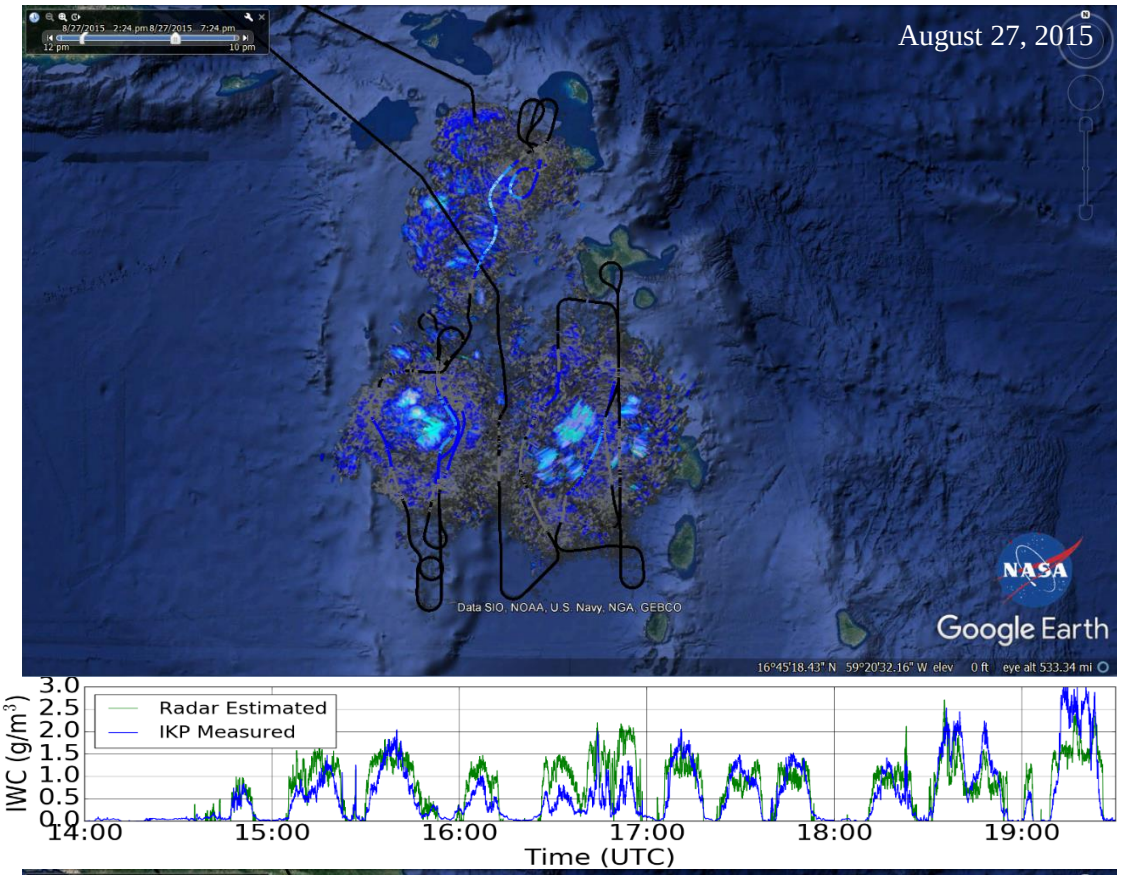
August 27, 2015
Data SIO, NOAA, U.S. Navy, NGA, GEBCO
Google Earth
16°45'18.43" N 59°20'32.16" W elev 0 ft eye alt 533.34 mi
Radar Estimated
IKP Measured
IWC (g/m³)
3.0
2.5
2.0
1.5
1.0
0.5
0.0
14:00
15:00
16:00
17:00
18:00
19:00
Time (UTC)

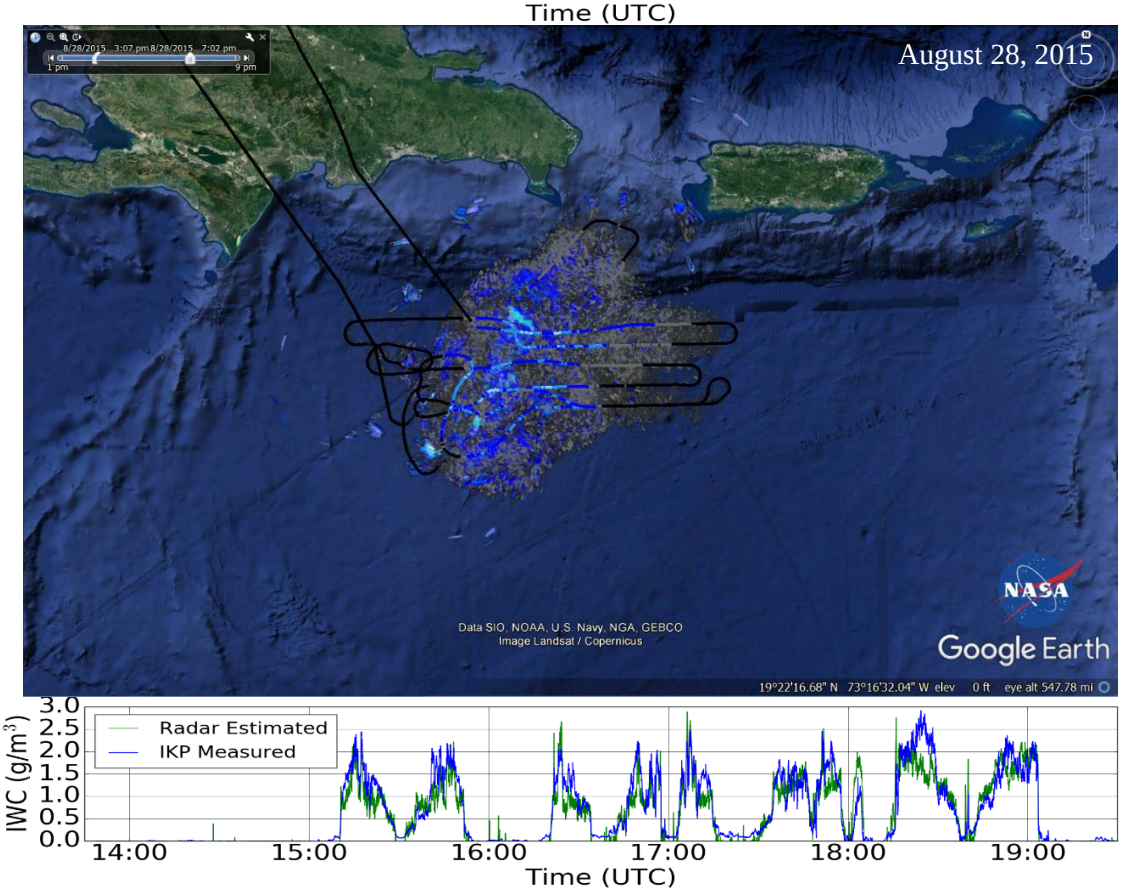
August 28, 2015
Data SIO, NOAA, U.S. Navy, NGA, GEBCO
Image Landsat / Copernicus
Google Earth
19°22'16.68" N 73°16'32.04" W elev 0 ft eye alt 547.78 mi
Radar Estimated
IKP Measured
IWC (g/m³)
3.0
2.5
2.0
1.5
1.0
0.5
0.0
14:00
15:00
16:00
17:00
18:00
19:00
Time (UTC)

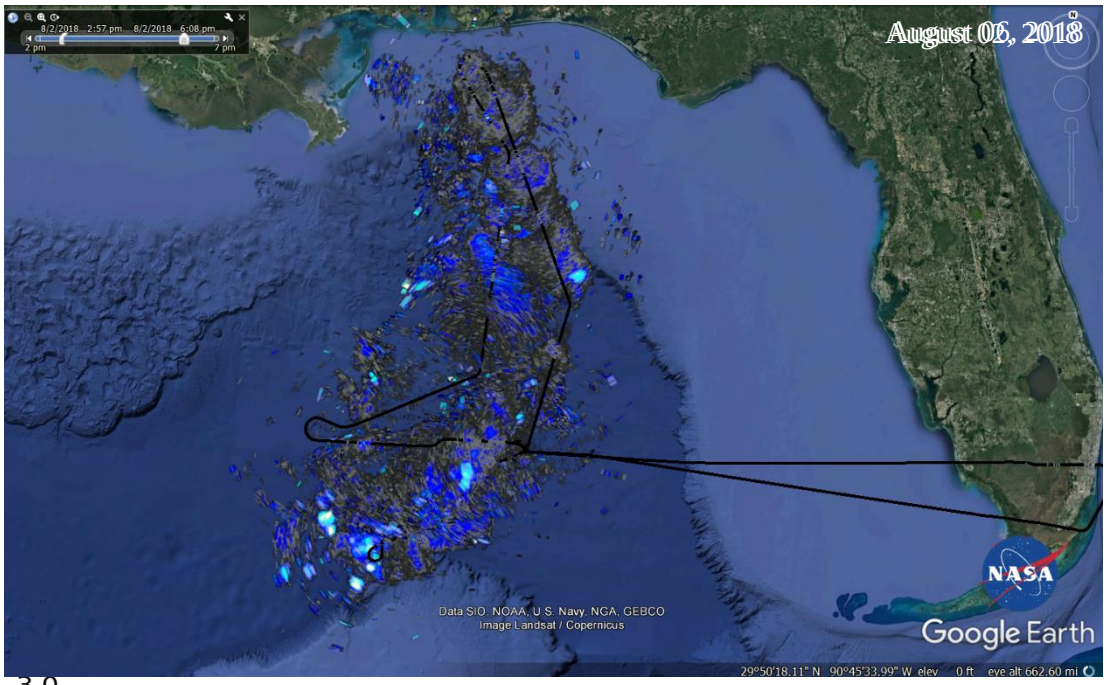
August 06, 2018
Data SIO, NOAA, U.S. Navy, NGA, GEBCO
Image Landsat / Copernicus
Google Earth

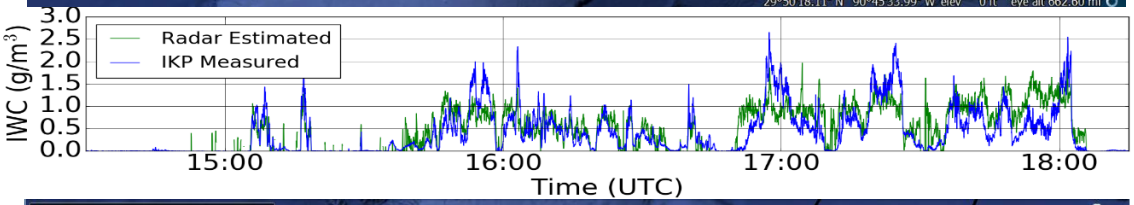
Radar Estimated
IKP Measured
IWC (g/m3)
3.0
2.5
2.0
1.5
1.0
0.5
0.0
15:00
16:00
17:00
18:00
Time (UTC)

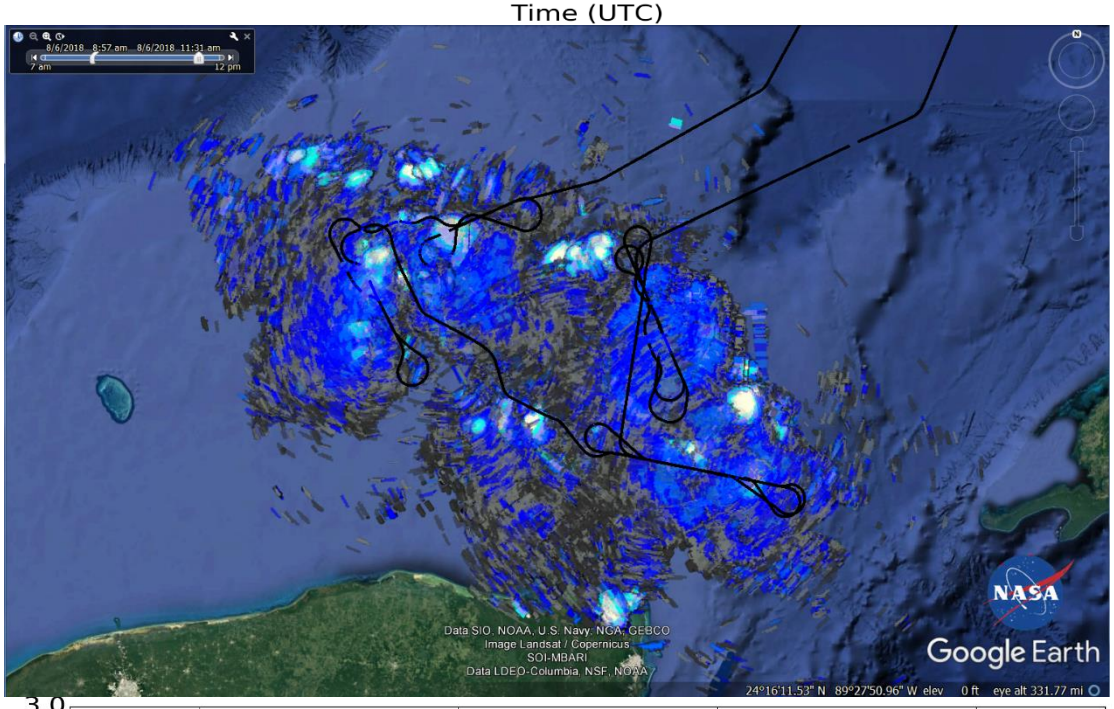
Data SIO, NOAA, U.S. Navy, NGA, GEBCO
Image Landsat / Copernicus
SOI-MBARI
Data LDEO-Columbia, NSF, NOAA
Google Earth

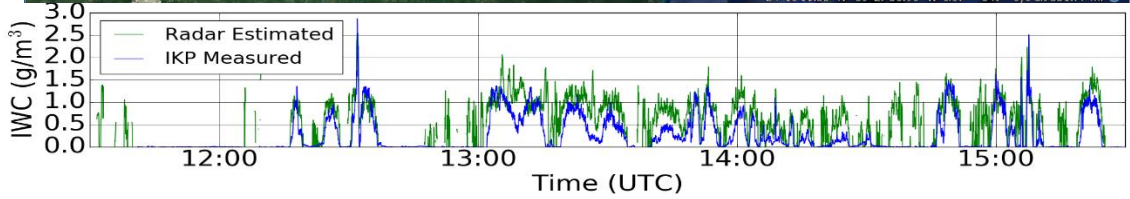
Radar Estimated
IKP Measured
IWC (g/m3)
3.0
2.5
2.0
1.5
1.0
0.5
0.0
12:00
13:00
14:00
15:00
Time (UTC)

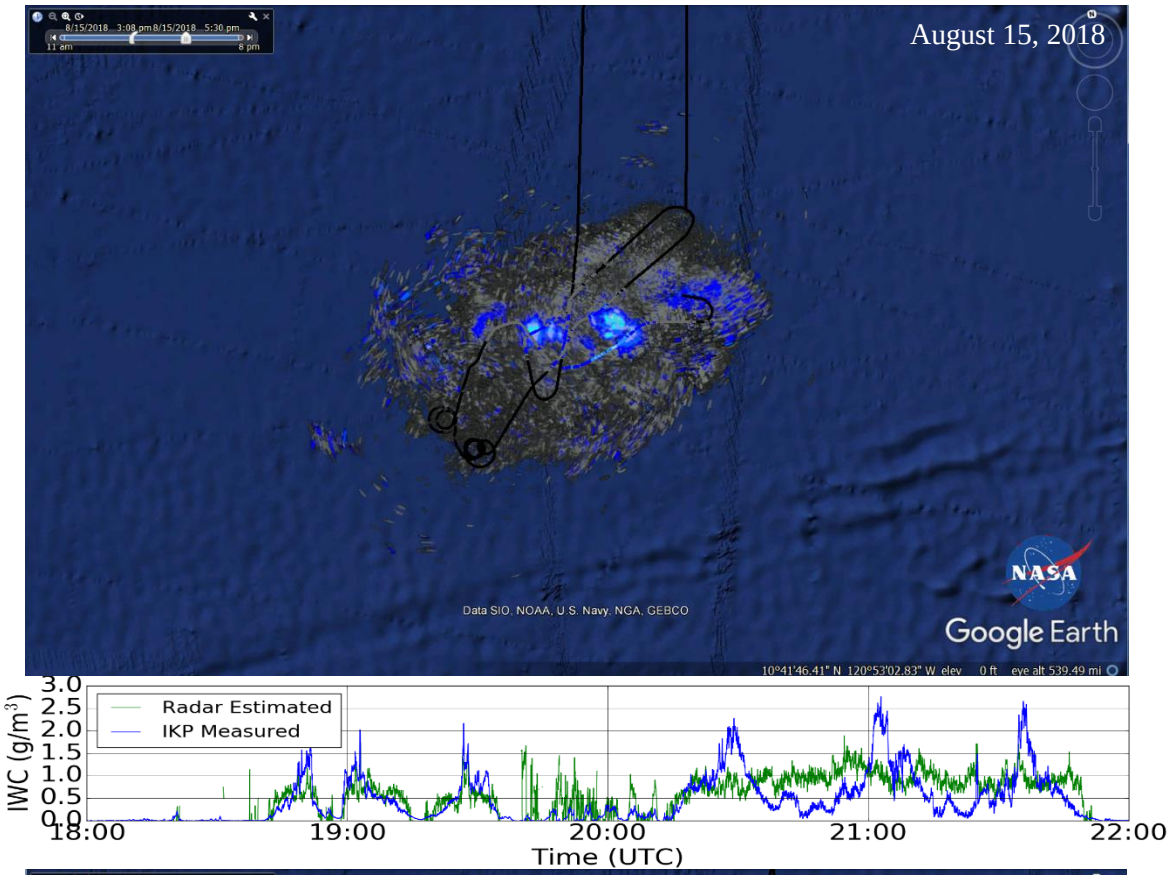
August 15, 2018
Data SIO, NOAA, U.S. Navy, NGA, GEBCO
Google Earth
Radar Estimated
IKP Measured
IWC (g/m3)
3.0
2.5
2.0
1.5
1.0
0.5
0.0
18:00
19:00
20:00
21:00
22:00
Time (UTC)

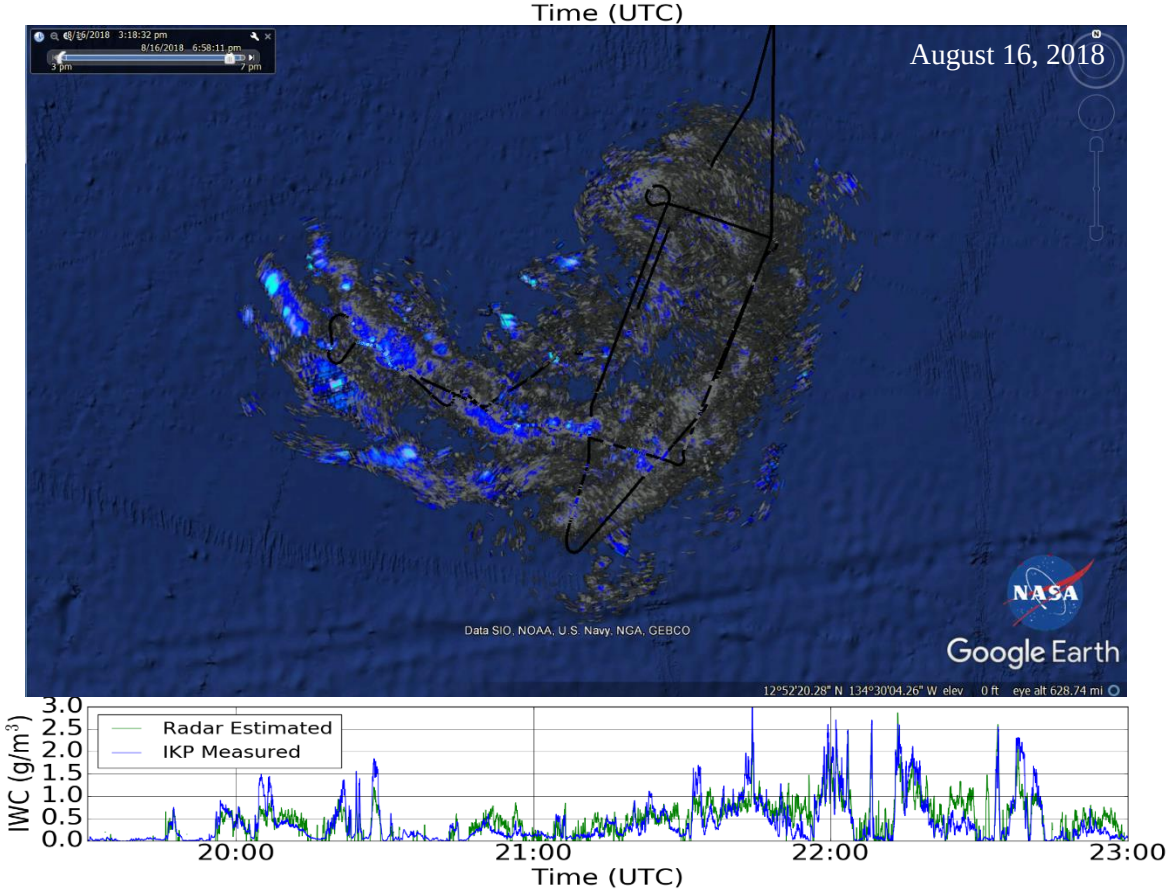
August 16, 2018
Data SIO, NOAA, U.S. Navy, NGA, GEBCO
Google Earth
Radar Estimated
IKP Measured
IWC (g/m3)
3.0
2.5
2.0
1.5
1.0
0.5
0.0
20:00
21:00
22:00
23:00
Time (UTC)

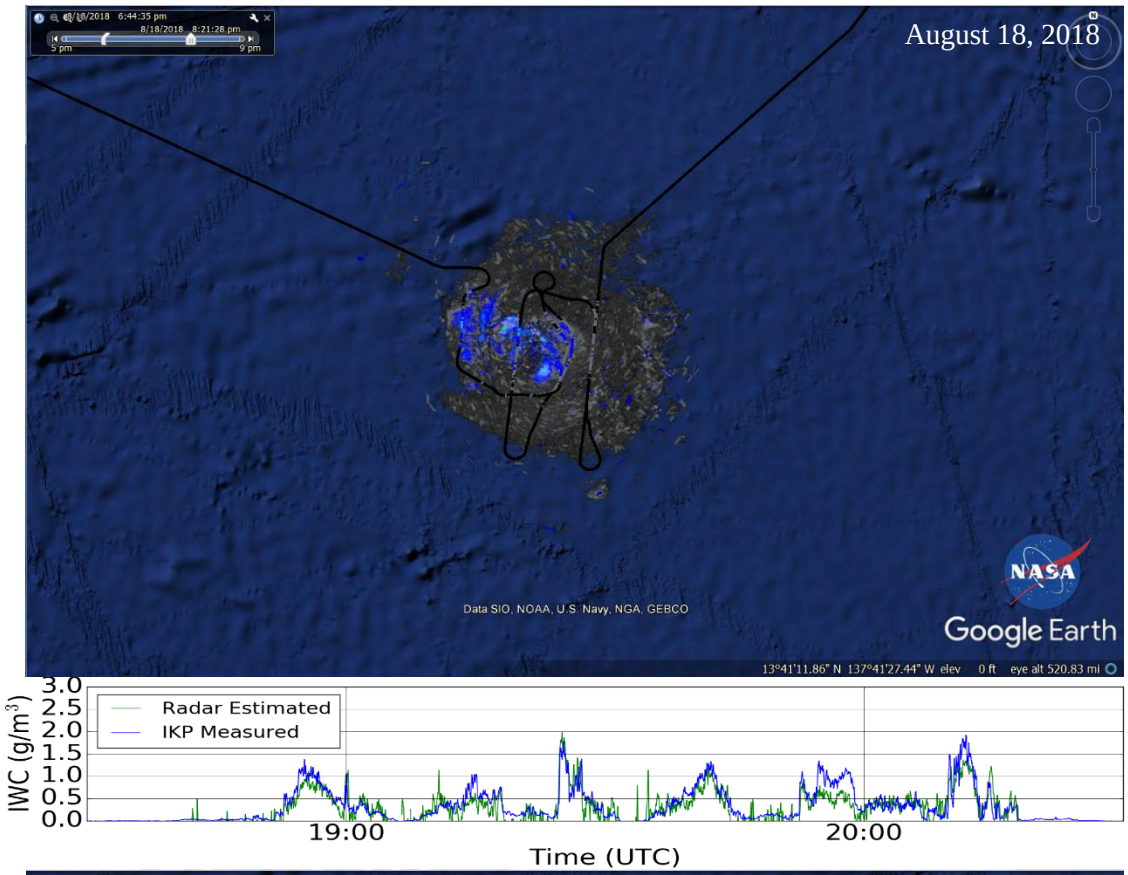
August 18, 2018
Data SIO, NOAA, U.S. Navy, NGA, GEBCO
Google Earth
Radar Estimated
IKP Measured
IWC (g/m3)
3.0
2.5
2.0
1.5
1.0
0.5
0.0
19:00
20:00
Time (UTC)

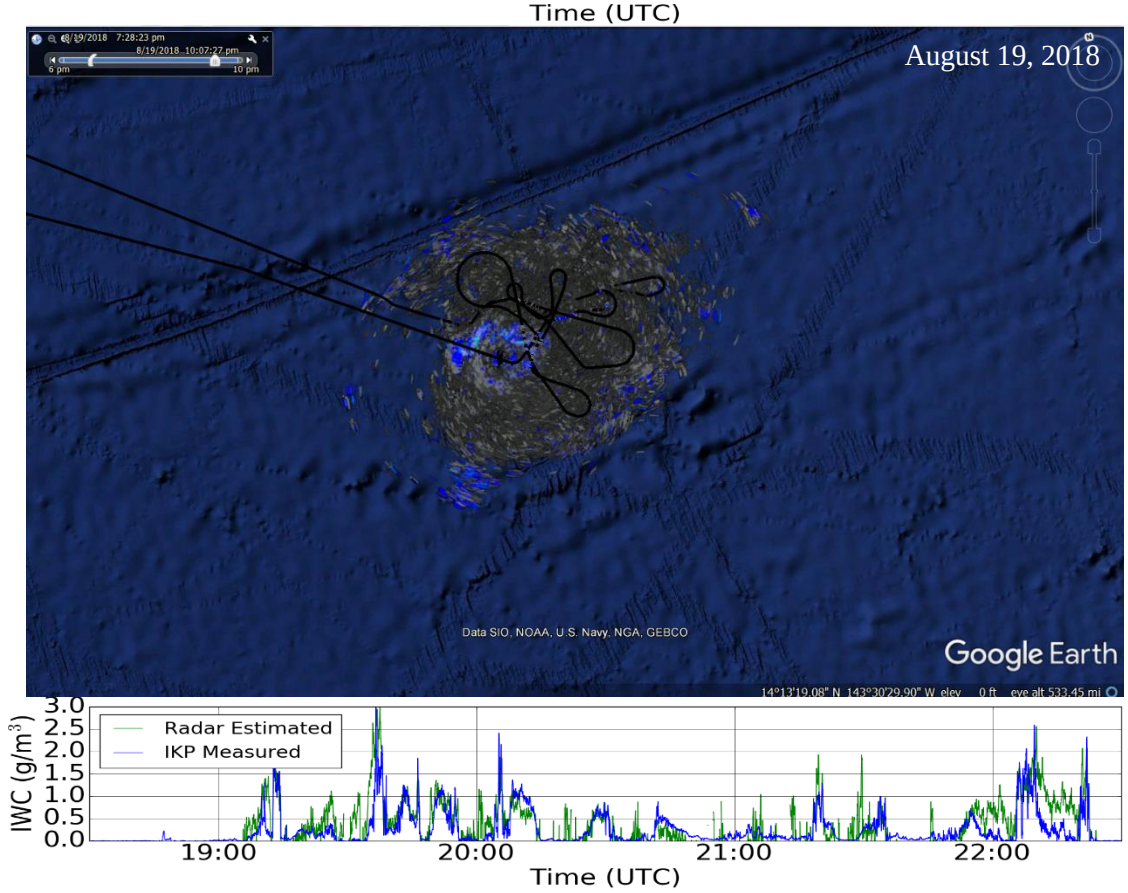
August 19, 2018
Data SIO, NOAA, U.S. Navy, NGA, GEBCO
Google Earth
Radar Estimated
IKP Measured
IWC (g/m3)
3.0
2.5
2.0
1.5
1.0
0.5
0.0
19:00
20:00
21:00
22:00
Time (UTC)

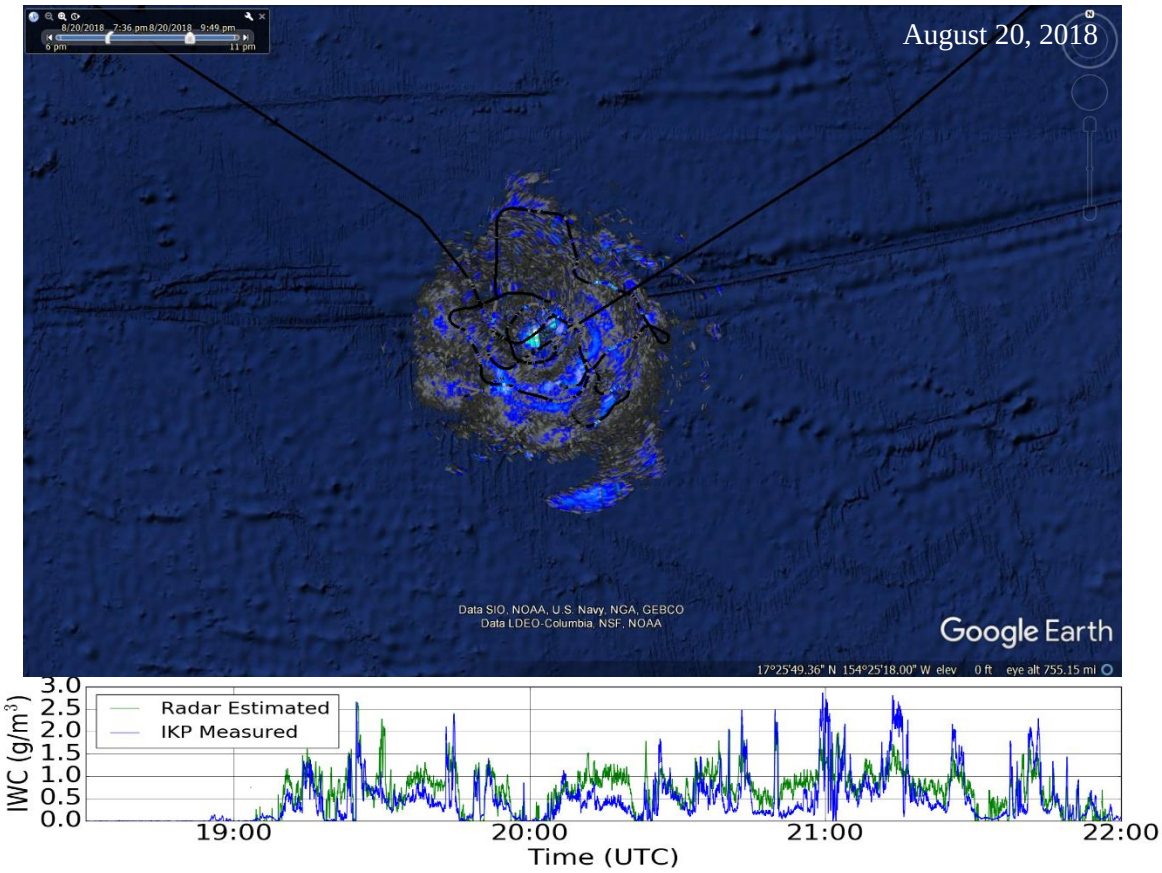
August 20, 2018
8/20/2018 7:36 pm 8/20/2018 9:49 pm
6 pm
11 pm
Data SIO, NOAA, U.S. Navy, NGA, GEBCO
Data LDEO-Columbia, NSF, NOAA
Google Earth
17°25'49.36" N 154°25'18.00" W elev 0 ft eye alt 755.15 mi
Radar Estimated
IKP Measured
IWC (g/m^3)
3.0
2.5
2.0
1.5
1.0
0.5
0.0
19:00
20:00
21:00
22:00
Time (UTC)

REPORT DOCUMENTATION PAGE

Form Approved
OMB No. 0704–0188

1. REPORT DATE *(DD-MM-YYYY)*	2. REPORT TYPE	3. DATES COVERED *(From - To)*
01-12-2019	Technical Publication	

4. TITLE AND SUBTITLE

Radar Detection of High Concentrations of Ice Particles – Methodology and Preliminary Flight Test Results

5a. CONTRACT NUMBER

5b. GRANT NUMBER

5c. PROGRAM ELEMENT NUMBER

6. AUTHOR(S)

Harrah, Steven; Strickland, Justin K.; Hunt, Patricia J.; Proctor, Fred H.; Switzer, George F.; Ratvasky, Tom; Strapp, Walter; Lilie, Lyle; Dumont, Chris

5d. PROJECT NUMBER

5e. TASK NUMBER

5f. WORK UNIT NUMBER

081876.02.07.50.08.01

7. PERFORMING ORGANIZATION NAME(S) AND ADDRESS(ES)

NASA Langley Research Center
Hampton, Virginia 23681-2199

8. PERFORMING ORGANIZATION REPORT NUMBER

L–21059

DOT/FAA/TC-19/29

9. SPONSORING/MONITORING AGENCY NAME(S) AND ADDRESS(ES)

National Aeronautics and Space Administration
Washington, DC 20546-0001

10. SPONSOR/MONITOR'S ACRONYM(S)

NASA

11. SPONSOR/MONITOR'S REPORT NUMBER(S)

NASA–TP–2019–220433

12. DISTRIBUTION/AVAILABILITY STATEMENT

Unclassified-Unlimited
Subject Category 03
Availability: NASA STI Program (757) 864-9658

13. SUPPLEMENTARY NOTES

14. ABSTRACT

High Ice Water Content (HIWC) has been identified as a primary causal factor in numerous engine events over the past two decades. Previous attempts to develop a remote detection process utilizing modern commercial radars have failed to produce reliable results. This paper discusses the reasons for previous failures and describes a new technique that has shown very encouraging accuracy and range performance without the need for any modifications to industry's current radar design(s). The performance of this new process was evaluated during the joint NASA/FAA HIWC RADAR II Flight Campaign in August of 2018. Results from that evaluation are discussed, along with the potential for commercial application, and development of minimum operational performance standards for a future commercial radar product.

15. SUBJECT TERMS

Aviation; Flight Test; Icing; Radar; Remote Sensing; Safety

16. SECURITY CLASSIFICATION OF:			17. LIMITATION OF ABSTRACT	18. NUMBER OF PAGES	19a. NAME OF RESPONSIBLE PERSON
a. REPORT	b. ABSTRACT	c. THIS PAGE			STI Help Desk (email: help@sti.nasa.gov)
U	U	U	UU	42	19b. TELEPHONE NUMBER *(Include area code)* (757) 864-9658